Isochrone fitting of Galactic globular clusters – IV. NGC 6362 and NGC 6723

George A. Gontcharov [1]★ Maxim Yu. Khovritchev [1,2] Aleksandr V. Mosenkov [1,3]
Vladimir B. Il'in [1,2,4] Alexander A. Marchuk [1,2] Denis M. Poliakov,[1,2] Olga S. Ryutina,[2]
Sergey S. Savchenko,[1,2,5] Anton A. Smirnov,[1,2] Pavel A. Usachev,[1,2,5] Jae-Woo Lee,[6] Conner Camacho [3]
and Noah Hebdon[3]

[1]*Central (Pulkovo) Astronomical Observatory, Russian Academy of Sciences, Pulkovskoye chaussee 65/1, St. Petersburg 196140, Russia*
[2]*Saint Petersburg State University, Universitetskij pr. 28, St. Petersburg 198504, Russia*
[3]*Department of Physics and Astronomy, Brigham Young University, N283 ESC, Provo, UT 84602, USA*
[4]*Saint Petersburg University of Aerospace Instrumentation, Bol. Morskaya ul. 67A, St. Petersburg 190000, Russia*
[5]*Special Astrophysical Observatory, Russian Academy of Sciences, 369167 Nizhnij Arkhyz, Russia*
[6]*Department of Physics and Astronomy, Sejong University, 209 Neungdo-ro, Gwangjin-Gu, Seoul 05006, Korea*

ABSTRACT

We present new isochrone fits to the colour–magnitude diagrams of the Galactic globular clusters NGC 6362 and NGC 6723. We utilize 22 and 26 photometric filters for NGC 6362 and NGC 6723, respectively, from the ultraviolet to mid-infrared using data sets from *Hubble Space Telescope*, *Gaia*, un*WISE*, and other photometric sources. We use models and isochrones from the Dartmouth Stellar Evolution Database (DSED) and Bag of Stellar Tracks and Isochrones (BaSTI) for α-enhanced $[\alpha/\text{Fe}] = +0.4$ and different helium abundances. The metallicities $[\text{Fe/H}] = -1.04 \pm 0.07$ and -1.09 ± 0.06 are derived from the red giant branch slopes in our fitting for NGC 6362 and NGC 6723, respectively. They agree with spectroscopic estimates from the literature. We find a differential reddening up to $\Delta E(B - V) = 0.13$ mag in the NGC 6723 field due to the adjacent Corona Australis cloud complex. We derive the following for NGC 6362 and NGC 6723, respectively: distances $7.75 \pm 0.03 \pm 0.15$ (statistic and systematic error) and $8.15 \pm 0.04 \pm 0.15$ kpc; ages $12.0 \pm 0.1 \pm 0.8$ and $12.4 \pm 0.1 \pm 0.8$ Gyr; extinctions $A_V = 0.19 \pm 0.04 \pm 0.06$ and $0.24 \pm 0.03 \pm 0.06$ mag; reddenings $E(B - V) = 0.056 \pm 0.01 \pm 0.02$ and $0.068 \pm 0.01 \pm 0.02$ mag. DSED provides systematically lower [Fe/H] and higher reddenings than BaSTI. However, the models agree in their relative estimates: NGC 6723 is 0.44 ± 0.04 kpc further, 0.5 ± 0.1 Gyr older, $\Delta E(B - V) = 0.007 \pm 0.002$ more reddened, and with 0.05 ± 0.01 dex lower [Fe/H] than NGC 6362. The lower metallicity and greater age of NGC 6723 with respect to NGC 6362 explain their horizontal branch morphology difference. This confirms age as the second parameter for these clusters. We provide lists of the cluster members from the *Gaia* Data Release 3.

Key words: Hertzsprung–Russell and colour–magnitude diagrams – globular clusters: general – globular clusters: individual: NGC 6362, NGC 6723 – dust, extinction.

1 INTRODUCTION

In recent years, the key ingredients for productive isochrone fitting of colour–magnitude diagrams (CMDs) of Galactic globular clusters (GCs) have been significantly improved. On the one hand, accurate photometry of individual stars in ultraviolet (UV), optical, and infrared (IR) bands has been obtained and presented in data sets from the *Hubble Space Telescope* (*HST*; Piotto et al. 2015; Nardiello et al. 2018; Simioni et al. 2018), *Gaia* Data Release 2 (DR2; Evans et al. 2018), and Early Data Release 3 (EDR3; Lindegren et al. 2021a; Riello et al. 2021), *Wide-field Infrared Survey Explorer* (*WISE*; Wright et al. 2010) as the un*WISE* catalogue (Schlafly et al. 2019), various ground-based telescopes by Stetson et al.

(2019, hereafter SPZ19), and other sources. On the other hand, theoretical stellar evolution models, such as the Dartmouth Stellar Evolution Database (DSED; Dotter et al. 2007)[1] and a Bag of Stellar Tracks and Isochrones (BaSTI; Pietrinferni et al. 2021),[2] have been upgraded for more accurate isochrones to predict CMDs with multiple low metallicity α-enhanced stellar populations with primordial or enriched helium abundance, which are typical in GCs (Monelli et al. 2013; Milone et al. 2017). Moreover, *Gaia* EDR3 provides very precise proper motions (PMs), which can be used for an accurate selection of GC members.

In Gontcharov, Mosenkov & Khovritchev (2019, hereafter Paper I; 2020, hereafter Paper II) and Gontcharov et al. (2021, hereafter

---

[1]http://stellar.dartmouth.edu/models/
[2]http://basti-iac.oa-abruzzo.inaf.it/index.html

Table 1. Some properties of the clusters under consideration. The *Gaia* EDR3 median parallax is calculated in Section 4.2.

Property	NGC 6362	NGC 6723
RA J2000 (h m s) from Goldsbury et al. (2010)	17 31 55	18 59 33
Dec. J2000 (° ′ ″) from Goldsbury et al. (2010)	$-67\ 02\ 54$	$-36\ 37\ 56$
Galactic longitude (°) from Goldsbury et al. (2010)	325.55452	0.06928
Galactic latitude (°) from Goldsbury et al. (2010)	-17.56977	-17.29893
Angular diameter (arcmin) from Bica et al. (2019)	19	17
Distance from the Sun (kpc) from Harris (1996), 2010 revision[3]	7.6	8.7
Distance from the Sun (kpc) from Baumgardt & Vasiliev (2021)	7.65 ± 0.07	8.27 ± 0.10
Gaia EDR3 median parallax (mas) from this study	0.1230 ± 0.011	0.1231 ± 0.011
[Fe/H] from Carretta et al. (2009)	-1.07 ± 0.05	-1.10 ± 0.07
Mean differential reddening $\overline{\Delta E(B-V)}$ (mag) from BCK13	0.025 ± 0.008	0.027 ± 0.009
Maximum differential reddening $\Delta E(B-V)_{max}$ (mag) from BCK13	0.046	0.051
$E(B-V)$ (mag) from Harris (1996), 2010 revision	0.09	0.05
$E(B-V)$ (mag) from SFD98	0.07	0.16
$E(B-V)$ (mag) from Schlafly & Finkbeiner (2011)	0.06	0.14
$E(B-V)$ (mag) from Meisner & Finkbeiner (2015)	0.11	0.13

[3]The commonly used database of GCs by Harris (1996) (https://www.physics.mcmaster.ca/~harris/mwgc.dat), 2010 revision.

Paper III), we fit CMDs for GCs NGC 288, NGC 362, NGC 5904 (M5), NGC 6205 (M13), and NGC 6218 (M12) by various isochrones for different stages of stellar evolution. They include the main sequence (MS), its turn-off (TO), the subgiant branch (SGB), red giant branch (RGB), horizontal branch (HB), and asymptotic giant branch (AGB). This fitting allows us to derive age, distance, and reddening for a dominant population or a mix of populations in each CMD, except for some in the UV and IR. Data set cross-identification allows us to estimate systematic differences between the data sets, convert the derived reddenings into extinctions in all the filters under consideration, and draw an empirical extinction law (i.e. a dependence of extinction on wavelength) for each combination of cluster, model and data set.

The pilot Paper I showed that such an approach is productive. In Paper II, we paid special attention to the balance of uncertainties in our approach (see also Section 3.1). In Paper III, we verified that a higher precision of the derived parameters can be achieved via an analysis of relative estimates for several similar GCs.

In this paper, we apply the same approach to the pair of GCs NGC 6362 and NGC 6723. This study is an enhancement of our approach due to the following: (i) these clusters are contaminated by foreground stars to a point where the data sets should be cleaned with PMs; (ii) NGC 6723 is affected by an adjacent foreground cloud complex; (iii) the clusters are similar in metallicity, age, distance, and reddening, which allow us to verify the sensitivity of our approach in an analysis of the relative estimates; (iv) the clusters are suitable for deriving [Fe/H] as a free parameter instead of adopting it from the literature.

As this is the fourth paper in this series, many details of our analysis, which we perform in this study, are given in our previous papers. We refer the reader to those papers, especially to the description of the balance of uncertainties, presented in appendix A of Paper II, creation of fiducial sequences (ridge lines), presented in Section 3 of Paper II, adjustment of different data sets with adjacent filters, presented in section 6 of Paper II, and usage of the *Gaia* EDR3 PMs and parallaxes for identification of cluster members, presented in section 3.2 of Paper III.

Previous isochrone fittings were done by Brocato et al. (1999), Piotto et al. (1999), Paust et al. (2010), Kerber et al. (2018) for NGC 6362, by Alcaino et al. (1999) for NGC 6723, and by Dotter et al. (2010), VandenBerg et al. (2013), O'Malley, Gilligan &

Chaboyer (2017), Wagner-Kaiser et al. (2017), Valcin et al. (2020), and Oliveira et al. (2020) for both the clusters. Their results can be compared with ours.

This paper is organized as follows. Some key properties of NGC 6362 and NGC 6723 are presented in Section 2. The theoretical models and corresponding isochrones, used for our isochrone-to-CMD fitting, as well as systematic uncertainties of the isochrones, are considered in Section 3. In Section 4, we describe the initial data sets used, their cleaning, cluster member identification, and fiducial sequence creation in the CMDs. In Section 5, we present and discuss the results of our isochrone fitting. We summarize our main findings and conclusions in Section 6. Some additional CMDs of the clusters are shown in Appendix A.

2 PROPERTIES OF THE CLUSTERS

Some general properties of NGC 6362 and NGC 6723 are presented in Table 1.

Each of the clusters has two populations (Dalessandro et al. 2014; Mucciarelli et al. 2016; Milone et al. 2017; Lee 2019). Both the populations of both the clusters are α-enriched with $0.3 < [\alpha/\text{Fe}] < 0.4$ (Rojas-Arriagada et al. 2016; Massari et al. 2017; Crestani et al. 2019). Milone et al. (2017) and Oliveira et al. (2020) estimate the fraction of the first (primordial) population of stars in NGC 6362 as 0.574 ± 0.035 and 0.584 ± 0.041, respectively, and 0.363 ± 0.017 and 0.377 ± 0.029 in NGC 6723, respectively. These estimates ensure that both the populations should be well represented in any CMD. The populations differ in helium abundance by $\Delta Y \approx 0.02$ or even 0.01 (Lagioia et al. 2018; Milone et al. 2018; VandenBerg & Denissenkov 2018; Lee 2019). Therefore, being well represented in a CMD, the populations are nevertheless segregated in colour or magnitude only in some domains of some CMDs, as discussed in Section 4.5. For an unresolved mix of the populations, which we meet in most CMD domains, we adopt the helium abundance $Y \approx 0.26$, i.e. 0.01 dex higher than $Y \approx 0.25$ for the primordial population.

Table 1 shows that NGC 6362 and NGC 6723 have moderately precise metallicity estimates. A large diversity of [Fe/H] estimates from the literature for both the clusters can be found in Lee et al. (2014), Kaluzhny et al. (2015), Arellano Ferro et al. (2018), VandenBerg & Denissenkov (2018), VandenBerg, Casagrande & Edvardsson (2022), and references therein: $-1.26 < [\text{Fe/H}] < -0.70$

for NGC 6362 and $-1.35 <$[Fe/H]<-0.93 for NGC 6723. Recent spectroscopic [Fe/H] estimates for NGC 6723 show a large variety as well: -1.22 ± 0.08 (Gratton et al. 2015), -0.98 ± 0.08 (Rojas-Arriagada et al. 2016), -0.93 ± 0.05 (Crestani et al. 2019). In contrast, recent spectroscopic [Fe/H] estimates for NGC 6362 are consistent: -1.09 ± 0.01 (Mucciarelli et al. 2016) and -1.07 ± 0.01 (Massari et al. 2017).

The slope of the RGB is sensitive to [Fe/H],[4] since the continuum opacity of RGB stars is mainly caused by the H$^-$ ion with the metals being the major donor of free electrons. This allows us to derive [Fe/H] as an isochrone fitting parameter (together with distance, age, and reddening) in CMDs with well-populated RGB in order to decrease fitting residuals. We then use our average [Fe/H] estimates for fitting the remaining CMDs. We do it separately for each model.

The RGBs are affected by saturation effects, crowding at the centres of the cluster fields, differential reddening, systematic errors of photometry, and helium enrichment (for the latter see Savino et al. 2018). All these effects may lead to a typical systematic uncertainty of about 0.15 dex in our [Fe/H] estimate derived from CMD and a model.

Although both the clusters show an extended HB, where both the blue and red sides of the RR Lyrae instability strip are populated, NGC 6362 and NGC 6723 are richer in red and blue HB stars, respectively. Their HB morphology is defined by their metallicity, as the most important parameter, and also by a yet unrecognized second parameter (see Crestani et al. 2019). Thus, the similarity of NGC 6362 and NGC 6723 makes them an interesting, albeit poorly investigated, second-parameter pair. In Paper III, we have shown that age may be the second parameter for NGC 288, NGC 362, NGC 5904, and NGC 6218. In this paper, we intend to answer whether age is the second parameter for NGC 6362 and NGC 6723 as well.

Table 1 shows a rather low foreground and differential reddening[5] for NGC 6362 and NGC 6723. However, the differential reddening, presented in Table 1, is estimated by Bonatto, Campos & Kepler (2013, hereafter BCK13) from *HST* ACS photometry within about 3.4 arcmin of the cluster centres, i.e. only in a small central part of the cluster field. Moreover, taking into account the stated precision of the reddening estimates in Table 1 as a few units of the last decimal place, the inconsistency of these estimates is evident.

An obvious source of this inconsistency for NGC 6723 is the adjacent Corona Australis cloud complex. This complex contains dark and bright nebulae: IC 4812, NGC 6729 around Herbig Ae/Be star R CrA, and a combination of NGC 6726 and NGC 6727 around Herbig Ae/Be star TY CrA. The latter is only 30 arcmin south (in Galactic coordinates) of NGC 6723. Periphery of this cluster is obscured by periphery of the nebula. This is seen in some Digital Sky Survey images and star counts, as discussed in Section 4.2. The reddening maps of Schlegel, Finkbeiner & Davis (1998, hereafter SFD98) and Meisner & Finkbeiner (2015) show $E(B - V) > 1.7$ mag in the centre of NGC 6726/NGC 6727 nebula. In contrast, $E(B - V) \approx 0.38$ and 0.11 mag on the edges of NGC 6723, at points nearest and farthest from the nebula, respectively (adopting the cluster diameter of 17 arcmin). In combination with the reddening estimates

$E(B - V) \approx 0.15$ mag from these maps for the NGC 6723 centre (see Table 1), these maps suggest a high and non-linear differential reddening in the NGC 6723 field.[6] Moreover, the brightness of the nebula parts is variable due to variability of TY CrA. This may lead to reddening estimate diversity in Table 1 if the estimates are obtained in different parts of the cluster field or in different moments. Surprisingly, to our knowledge, the Corona Australis cloud complex has never been considered as a source of differential reddening in the NGC 6723 field. For example, Hendricks et al. (2012, hereafter HSV12) described this cluster as 'nearly unreddened GC NGC 6723'.

3 THEORETICAL MODELS AND ISOCHRONES

To fit the CMDs of NGC 6362 and NGC 6723, we use the following theoretical models of stellar evolution and related α-enhanced isochrones:

(i) BaSTI (Hidalgo et al. 2018; Pietrinferni et al. 2021) with various [Fe/H], helium abundance $Y = 0.25$ for primordial and 0.275 for helium-enriched population, [α/Fe] $= +0.4$, initial solar $Z_\odot = 0.0172$ and $Y_\odot = 0.2695$, overshooting, diffusion, mass-loss efficiency $\eta = 0.3$, where η is the free parameter in Reimers law (Reimers 1975). We draw both the BaSTI isochrones with $Y = 0.25$ and 0.275 in all our CMD figures, while the interpolated isochrones with $Y = 0.26$ are not drawn for clarity. As in Paper III, we also use the BaSTI extended set of zero-age horizontal branch (ZAHB) models with different values of the total mass but the same mass for the helium core and the same envelope chemical stratification. This set presents a realistic description of stochastic mass-loss between the MS and HB, when stars with the same mass during the MS can lose different amounts of mass during the RGB and, hence, differ in their colours and magnitudes during the HB. This BaSTI set of ZAHB models appears very important for appropriate HB fitting.

(ii) DSED (Dotter et al. 2008) with various [Fe/H], helium abundance $Y = 0.25$ for primordial and 0.33 for helium-enriched population, [α/Fe] $= +0.4$, solar $Z_\odot = 0.0189$ and no mass-loss. We use the $Y = 0.25$ and 0.33 isochrones in order to interpolate intermediate isochrones (DSED provides no α-enhanced isochrone for $0.25 < Y < 0.33$). Naturally, the isochrones with $Y = 0.25$ and $Y = 0.26$ are close to each other, while $Y = 0.33$ seems to overestimate the helium enrichment of these clusters (see Section 2). DSED gives no prediction for the HB and AGB. DSED does not provide isochrones for VISTA filters. However, we have verified that J_{VISTA} can be substituted by J_{UKIDSS}, a filter from the United Kingdom Infrared Telescope Infrared Deep Sky Survey (UKIDSS; Hewett et al. 2006), with a precision better than 0.01 mag. We use the DSED isochrones for J_{UKIDSS} instead of J_{VISTA}, while there is no DSED substitution for Ks_{VISTA} filter.

DSED and BaSTI are models that provide user-friendly online tools to calculate α-enhanced isochrones for various levels of helium enrichment and almost all filters under consideration, using stellar metallicity, age, and mass as input. Hereafter, we use only DSED and BaSTI α-enhanced isochrones. This is in line with, e.g. the isochrone fitting of the same clusters by Oliveira et al. (2020).

We consider the isochrones for a grid of some reasonable [Fe/H] with a step of 0.05 dex, distances with a step of 0.1 kpc, reddenings with a step of 0.001 mag, and ages over 8 Gyr with a step of 0.5 Gyr.

---

[4]The same is also true for the faint MS, about >4 mag fainter than TO. However, isochrones have large systematic uncertainties in the faint MS domain. Hence, we do not consider this domain at all.

[5]In this paper, we consider differential reddenings as systematic variations of colours in a cluster field due to variations of reddening, as well as due to other reasons, as discussed by Anderson et al. (2008) and in Paper III. For NGC 6723, variations of reddening certainly dominate in systematic variations of colours in the cluster field.

[6]For comparison, for NGC 6362 the SFD98 map shows only $\Delta E(B - V) < 0.01$ mag over the whole cluster field. Hence, we do not need a differential reddening correction for NGC 6362.

In contrast to our previous studies, we derive [Fe/H] as an isochrone fitting parameter (together with distance, age, and reddening) in CMDs with a rich bright RGB (Table 6 shows the derived [Fe/H] estimates) and then use our average [Fe/H] estimates (separately for each model) for fitting the remaining CMDs.

The derived [Fe/H] are discussed and compared with those avaliable in the literature in Section 5.3.

3.1 Systematics from isochrones

Systematic errors from stellar modelling, bolometric corrections, and colour versus effective temperature (T_{eff}) relations should be revealed in (i) comparison of different isochrones in their fitting to similar data sets (model-to-model differences), (ii) comparison of cluster parameter estimates from different studies (study-to-study differences), (iii) theoretical evaluation of intrinsic uncertainty in each isochrone prediction ingredient and their unification. The latter approach should be realized by the authors of models, while the others can be briefly realized here.

On the one hand, the only manifestation of the DSED and BaSTI model-to-model systematics in our final results is a systematically lower metallicity (by about [Fe/H] = 0.12 dex) through DSED (see Section 5.3). The lower the metallicity the bluer the isochrone. Hence, by DSED, a lower [Fe/H] leads to systematically higher reddenings of about $\Delta E(B - V) = 0.02$ mag. On the other hand, a study-to-study scatter of recent spectroscopic [Fe/H] measurements shows ±0.14 dex for NGC 6723 and reads much lower for NGC 6362 (see Section 1). Therefore, assuming uncertainty of adopted [Fe/H] as the dominant contributor to uncertainty of reddening and extinction, we assign a systematic uncertainty corresponding to $\sigma E(B - V) = 0.02$ or $\sigma A_V = 0.06$ to all our reddening/extinction results.

Both the model-to-model and the study-to-study comparison shows a rather large systematic uncertainty of age. For example, a typical difference between age estimates, obtained for similar data sets by similar methods, from Dotter et al. (2010), Wagner-Kaiser et al. (2017), Kerber et al. (2018), Oliveira et al. (2020), and Valcin et al. (2020) is up to ±0.8 Gyr. VandenBerg & Denissenkov (2018) noted that the age uncertainty is ±0.8 Gyr, 'of which ±0.5 Gyr is due to a ±0.05 mag uncertainty in the distance modulus and the rest corresponds to the net effect of metal abundance uncertainties'. Oliveira et al. (2020) noted 'a conservative uncertainty of 0.5 Gyr in the ages can be adopted due to chemical abundance uncertainties'. Valcin et al. (2020) noted 'In total, we have a 0.5 Gyr uncertainty budget due to systematic effects in stellar modelling'. The difference of about 0.7 Gyr between the results of the single- and two-population analysis of Wagner-Kaiser et al. (2016, 2017) for the same clusters may be another manifestation of large systematic uncertainties. Finally, we assign 0.8 Gyr as a conservative systematic uncertainty of our derived ages.

All recent (since VandenBerg et al. 2013) estimates of the distance modulus for NGC 6362 using isochrone-to-CMD fitting, are within 14.36–14.45 (including our own 14.45 from Section 5). Those for NGC 6723 are within 14.53–14.59. Taking into account the discussion in Valcin et al. (2020) and the conclusion of VandenBerg et al. (2022) 'isochrones generally reproduce the main features of observed CMDs to within ≈0.03 mag', we adopt a systematic uncertainty of distance moduli as ±0.04. This converts to ±150 pc distance uncertainty for our clusters.

It is worth noting that if we adopt a systematic uncertainty from a study-to-study comparison, then, naturally, our result with this systematic uncertainty agrees with all the stuidies and, hence, *a*

posteriori comparison of our result with those from the studies has little sense.

4 DATA SETS

4.1 Initial data sets

We use the following data sets for both the clusters (hereafter *twin* data sets) – see Table 2:

(i) the *HST* Wide Field Camera 3 (WFC3) UV Legacy Survey of Galactic GCs (the *F275W*, *F336W*, and *F438W* filters) and the Wide Field Channel of the Advanced Camera for Surveys (ACS; the *F606W* and *F814W* filters) survey of Galactic globular clusters (Piotto et al. 2015; Nardiello et al. 2018),[7][8]

(ii) photometry from Piotto et al. (2002) in the *F439W* and *F555W* filters from the *HST* Wide Field and Planetary Camera 2 (WFPC2),

(iii) *UBVRI* photometry described by SPZ19,[9] with the NGC 6362 and NGC 6723 data sets processed within the same pipeline and presented recently,[10]

(iv) *Gaia* DR2 and EDR3 photometry in the G, G_{BP}, and G_{RP} filters (Evans et al. 2018; Riello et al. 2021),[11]

(v) SkyMapper Southern Sky Survey DR3 (SMSS, SMSS DR3) photometry in the g_{SMSS}, r_{SMSS}, i_{SMSS}, and z_{SMSS} filters (Onken et al. 2019),[12]

(vi) J_{VISTA} and Ks_{VISTA} photometry of the VISTA Hemisphere Survey with the VIRCAM instrument on the Visible and Infrared Survey Telescope for Astronomy (VISTA,VHS DR5; (McMahon et al. 2013)),[13]

(vii) *WISE* photometry in the *W*1 filter from the unWISE catalogue (Schlafly et al. 2019).[14]

Also, we use the following data sets for one of the clusters (see Table 2):

(i) *BV* photometry of NGC 6362 with the 2.5-m du Pont telescope of Las Campanas Observatory (Zloczewski et al. 2012, hereafter ZKR12),[15]

(ii) *BV* photometry of NGC 6362 with the 1-m Swope telescope of Las Campanas Observatory (Narloch et al. 2017, hereafter NKP17),[16]

(iii) *V* and Strömgren *by* photometry of NGC 6723 with the Cerro Tololo Inter-American Observatory (CTIO) 1-m telescope (Lee 2019).

---

[7] http://groups.dfa.unipd.it/ESPG/treasury.php

[8] We do not use the *HST* ACS photometry from Simioni et al. (2018) due to its sparsely populated RGB, SGB, and TO.

[9] http://cdsarc.u-strasbg.fr/viz-bin/cat/J/MNRAS/485/3042

[10] https://www.canfar.net/storage/vault/list/STETSON/homogeneous/Latest_photometry_for_targets_with_at_least_BVI

[11] We consider DR2, since DSED provides its valuable isochrones only for DR2 but not for EDR3. We compare the colours and magnitudes of the cluster stars, common in DR2 and EDR3, and find no significant systematic difference. Accordingly, the DSED isochrones for DR2 are equally suitable for EDR3 and, hence, shown in our CMDs with the EDR3 data. Therefore, we do not present our results obtained with DR2. Note that the photometry and astrometry of these clusters is exactly the same in *Gaia* EDR3 and DR3.

[12] https://skymapper.anu.edu.au

[13] https://cdsarc.cds.unistra.fr/viz-bin/ReadMe/II/367?format=html&tex = true

[14] https://cdsarc.cds.unistra.fr/viz-bin/cat/II/363

[15] https://cdsarc.cds.unistra.fr/viz-bin/cat/J/AcA/62/357

[16] https://cdsarc.cds.unistra.fr/viz-bin/cat/J/MNRAS/471/1446

Table 2. The effective wavelength λ_{eff} (nm), number of stars and median precision of the photometry (mag) for the data sets and filters under consideration. The number of *Gaia* cluster members among the SPZ19 and Lee (2019) data sets is shown in brackets.

Telescope, data set, and reference	Filter	λ_{eff}	Number of stars/median precision	
			NGC 6362	NGC 6723
HST/WFC3 (Nardiello et al. 2018)	*F275W*	285	5692/0.02	14 842/0.02
HST/WFC3 (Nardiello et al. 2018)	*F336W*	340	7863/0.02	19 886/0.02
Various (SPZ19)	*U*	366	14 527 (4651)/0.02	15 113 (3309)/0.02
HST/WFC3 (Nardiello et al. 2018)	*F438W*	438	8518/0.01	20512/0.01
HST/WFPC2 (Piotto et al. 2002)	*F439W*	439	3275/0.04	4319/0.06
Various (SPZ19)	*B*	452	18546 (4803)/0.01	22 489 (3398)/0.01
2.5-m du Pont telescope, Las Campanas (ZKR12)	*B*	452	9568/0.01	–
1-m Swope telescope, Las Campanas (NKP17)	*B*	452	13 484/0.02	–
1-m CTIO telescope (Lee 2019)	Strömgren *b*	469	–	27 206 (4765)/0.02
SkyMapper Sky Survey DR3 (Onken et al. 2019)	g_{SMSS}	514	2063/0.02	877/0.02
Gaia EDR3 (Riello et al. 2021)	G_{BP}	523	5069/0.02	2207/0.03
1-m CTIO telescope (Lee 2019)	Strömgren *y*	550	–	27 206 (4765)/0.02
HST/WFPC2 (Piotto et al. 2002)	*F555W*	551	3275/0.04	4319/0.05
Various (SPZ19)	*V*	552	18 933 (4803)/0.01	23 867 (3398)/0.01
1-m CTIO telescope (Lee 2019)	*V*	552	–	27 206 (4765)/0.02
2.5-m du Pont telescope, Las Campanas (ZKR12)	*V*	552	9568/0.01	–
1-m Swope telescope, Las Campanas (NKP17)	*V*	552	13 484/0.02	–
NTT, ESO, La Silla (HSV12)	*V*	552	–	Fiducial/0.03
HST/ACS (Nardiello et al. 2018)	*F606W*	599	21 059/0.01	38 689/0.01
SkyMapper Sky Survey DR3 (Onken et al. 2019)	r_{SMSS}	615	2139/0.02	977/0.02
Gaia EDR3 (Riello et al. 2021)	*G*	628	5069/0.01	2207/0.01
Various (SPZ19)	*R*	659	16681 (4614)/0.01	21 838 (3359)/0.01
Gaia EDR3 (Riello et al. 2021)	G_{RP}	770	5069/0.02	2207/0.03
SkyMapper Sky Survey DR3 (Onken et al. 2019)	i_{SMSS}	776	1545/0.02	1285/0.02
HST/ACS (Nardiello et al. 2018)	*F814W*	807	20 978/0.01	38 208/0.01
Various (SPZ19)	*I*	807	18 698 (4802)/0.01	24 356 (3398)/0.01
SkyMapper Sky Survey DR3 (Onken et al. 2019)	z_{SMSS}	913	1202/0.02	1108/0.02
NTT, ESO, La Silla (HSV12)	J_{2MASS}	1234	–	Fiducial/0.03
VISTA VHS DR5 (McMahon et al. 2013)	J_{VISTA}	1277	4401/0.05	2261/0.03
VISTA VHS DR5 (McMahon et al. 2013)	Ks_{VISTA}	2148	2898/0.10	1927/0.09
NTT, ESO, La Silla (HSV12)	Ks_{2MASS}	2176	–	Fiducial/0.03
WISE, unWISE (Schlafly et al. 2019)	*W*1	3317	505/0.02	504/0.01

(iv) the fiducial sequences for NGC 6723 in the *V*, J_{2MASS}, and Ks_{2MASS} filters derived by HSV12 from the photometry with the New Technology Telescope (NTT) of European Southern Observatory (ESO), La Silla, transformed to the Two Micron All Sky Survey (2MASS) photometric system (Skrutskie et al. 2006).

(v) the fiducial sequences for NGC 6723 in the *UBVRI* filters derived by Alcaino et al. (1999) from the photometry with the 2.5-m du Pont telescope of Las Campanas Observatory. Finally, we reject the Alcaino et al. (1999)'s data set (see Section 4.3) because of its strong systematics due to non-member contamination.

The SPZ19 data sets include photometry from various initial data sets, but not from ZKR12, NKP17, or Alcaino et al. (1999).

Each star has photometric data in some but not all filters. In total, 22 and 26 filters are used for NGC 6362 and NGC 6723, respectively. They span a wide wavelength range between the UV and middle IR. For each filter, Table 2 indicates the effective wavelength λ_{eff} in nm, number of stars and the median photometric precision after the cleaning of the data set. Before the cleaning, the initial data sets contained many more stars. The median precision is calculated from the precisions stated by the authors of the data sets. We use the median precision for calculating predicted uncertainties of the derived [Fe/H], age, distance and reddening, as described in appendix A of Paper II and Section 5.

NGC 6362 and NGC 6723 are not so rich in photometric data as the GCs from our previous papers. However, several twin data sets of accurate photometry are available for both the clusters. NGC 6362 and NGC 6723 are rather similar in their distance from the Sun, age, reddening, [Fe/H], and HB morphology. Therefore, they are suitable to consider relative estimates of these parameters in the form 'NGC 6723 minus NGC 6362', separately derived for each model, from an isochrone fitting to each pair of the twin data sets. Some systematic errors of the models dominate in final absolute estimates of the parameters (see Section 3.1). These systematic errors are canceled out in such relative estimates. Hence, we expect the relative estimates to be much more accurate than the absolute ones.

Some initial samples/data sets are selected by use of the VizieR and X-Match services of the Centre de Données astronomiques de Strasbourg (Ochsenbein, Bauer & Marcout 2000).[17] As described in Section 4.2, the *Gaia* EDR3 data sets are selected within wide areas in order to identify cluster members and derive empirical truncation radii of 10 and 8.5 arcmin for NGC 6362 and NGC 6723, respectively. These radii are used to select or truncate the other data sets.

Cleaning of the data sets is similar to that done for GCs in Paper III. Typically, we select stars with a photometric error of less than 0.1 mag. However, some data sets have an initial error limit of <0.1. Also the 0.08 mag error limit is applied to the data sets of Nardiello et al. (2018) for NGC 6723 in the *F438W*, *F606W*, and *F814W* bands,
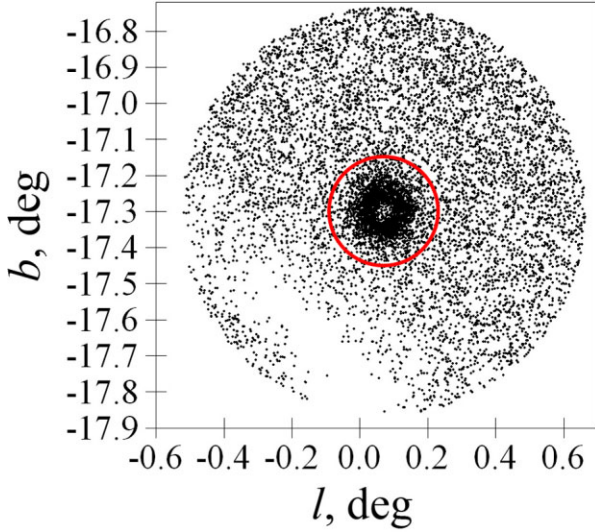
---

[17]http://cds.u-strasbg.fr

Figure 1. The distribution of the initial *Gaia* EDR3 data set for NGC 6723 in the sky in Galactic coordinates within 34 arcmin from the cluster centre. The red circle shows the selection area within 8.5 arcmin from the cluster centre.

Gaia EDR3, and NKP17; the 0.2 mag limit – to the VISTA Ks_{VISTA} photometry.

For the data sets of SPZ19 we select stars with `DAOPHOT` parameters $\chi < 3$ and $|sharp| < 0.3$. For the *HST* WFC3 and ACS photometry, we select stars with $|sharp| < 0.15$, membership probability >0.9 or -1, and quality fit >0.9. For the NKP17 data set, we select stars with a cluster member probability higher than 0.5. For the ZKR12 data set, we select 'likely members'. For the *Gaia* DR2 data sets, we select stars with photometry in all three *Gaia* bands and an acceptable parameter `phot_bp_rp_excess_factor` $< 1.3 + 0.06\,\text{bp\_rp}^2$, as suggested by Evans et al. (2018).

Gaia EDR3 stars with a precise photometry are selected as those with available data in all three *Gaia* bands, with a normalized unit weight error not exceeding 1.4 (`RUWE < 1.4`), and an acceptable corrected excess factor `phot_bp_rp_excess_factor` (i.e. `E(BP/RP)Corr`) between -0.14 and 0.14 (Riello et al. 2021). Unfortunately, this cleaning of the *Gaia* EDR3 data sets removes almost all stars in a central arcminute of both the cluster fields. The remaining stars at the centres do not show any systematics in CMDs. Note that the identification of *Gaia* cluster members (see Section 4.2) does not use any photometric data and, hence, is fulfilled before the cleaning of the *Gaia* EDR3 data sets.

4.2 *Gaia* EDR3 cluster members

Similar to Paper III, we use accurate PMs and parallaxes from *Gaia* EDR3 to select cluster members and calculate systemic cluster PMs and parallaxes. Here, we briefly summarize this procedure.

First, we select initial *Gaia* EDR3 samples within initial radii which are six and four times larger than the halved diameters in Table 1 for NGC 6362 and NGC 6723, respectively. The latter is smaller in order to avoid the highly extincted sky region of the Corona Australis cloud complex near NGC 6723 (see Section 2 and 4.4). Yet, even within 34 arcmin from the NGC 6723 centre, the complex strongly obscures the *Gaia* EDR3 stars. This is seen in Fig. 1 as the void in the distribution of the initial *Gaia* EDR3 data set for NGC 6723. The red circle shows the finally adopted truncation radius.
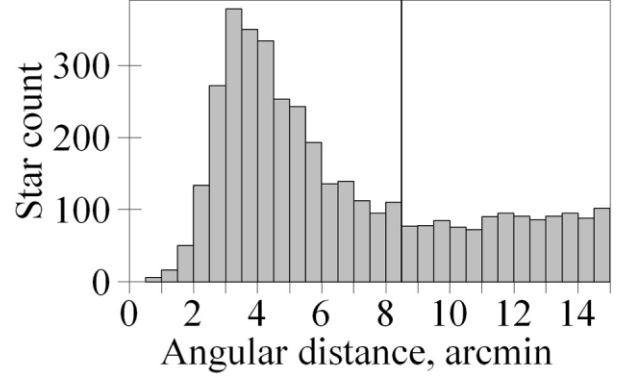

Figure 2. The distribution of the initial *Gaia* EDR3 data set for NGC 6723 along the angular distance from the cluster centre. The vertical line shows the truncation radius of 8.5 arcmin.

Second, the periphery of the initial field is used for estimating the star count surface density of the Galactic background. Its subtraction allows us to determine the empirical truncation radii of 10 and 8.5 arcmin for NGC 6362 and NGC 6723, respectively. A star count transition from the background to NGC 6723 at 8.5 arcmin from its centre is presented in Fig. 2. These truncation radii are very close to the halved diameters presented in Table 1. Few, if any, cluster members should be outside these radii. Therefore, in order to reduce contamination by non-members, we truncate all the data sets under consideration at these radii (except for data sets with fiducial sequences only).

Thirdly, we reject few stars without PMs and leave only *Gaia* EDR3 stars with `duplicated_source = 0` (`Dup = 0`) and `astrometric_excess_noise < 1` ($\epsilon i < 1$). We reject foreground and background stars as those with measured parallax $\varpi > 1/R + 3\sigma_\varpi$ or $\varpi < 1/R - 3\sigma_\varpi$, where σ_ϖ is the stated parallax uncertainty, while R is our estimate of the distance to the cluster. The latter is upgraded iteratively starting from the Baumgardt & Vasiliev (2021) values in Table 1.

Fourth, we adopt initial cluster centre coordinates from Goldsbury et al. (2010) and initial systemic PM components $\overline{\mu_\alpha \cos(\delta)}$ and $\overline{\mu_\delta}$ from Vasiliev & Baumgardt (2021, hereafter VB21). Then we calculate the standard deviations $\sigma_{\mu_\alpha \cos(\delta)}$ and σ_{μ_δ} of the PM components $\mu_\alpha \cos(\delta)$ and μ_δ for the cluster members. We cut-off the sample at 3σ, i.e. select cluster members as stars with

$$\sqrt{(\mu_\alpha \cos(\delta) - \overline{\mu_\alpha \cos(\delta)})^2 + (\mu_\delta - \overline{\mu_\delta})^2} < 3\sqrt{\sigma^2_{\mu_\alpha \cos(\delta)} + \sigma^2_{\mu_\delta}}.$$

Then we recalculate the mean coordinates of the cluster centre and weighted mean systemic PM components. This procedure is repeated iteratively until we stop losing stars in the 3σ cut.

Note that since the stated *Gaia* EDR3 PM uncertainty increases strongly with magnitude, faint cluster members make a negligible contribution to the weighted mean systemic PMs.

The final empirical standard deviations $\sigma_{\mu_\alpha \cos(\delta)}$ and σ_{μ_δ} are reasonable, being slightly higher than the mean stated PM uncertainties: 0.25 versus 0.17 and 0.34 versus 0.27 mas yr^{-1} for NGC 6362 and NGC 6723, respectively (averaged for the PM components). Fig. 3 shows a distribution of stars, selected within 8.5 arcmin of the NGC 6723 centre, over the PM components, after the remaining cleaning of the sample (see Section 4.1). The cluster members are those inside the red circle. The CMD of the stars from Fig. 3 is shown in Fig. 4.

Table 3 presents our final weighted mean PMs in comparison to those from VB21 and Vitral (2021). They are also derived from *Gaia*
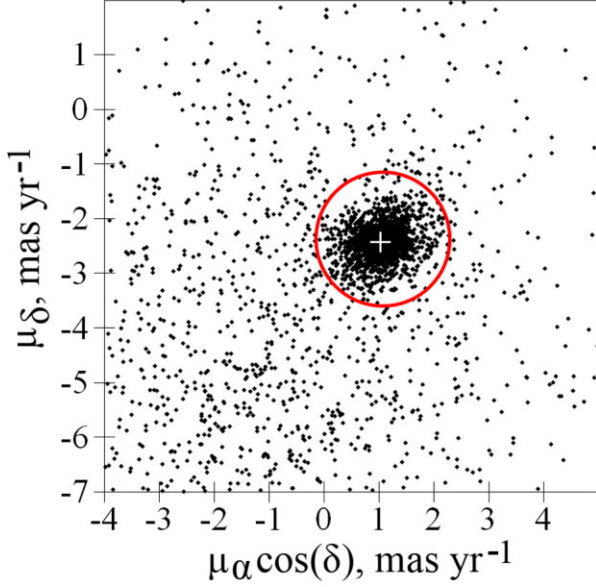
Figure 3. The distribution of stars, selected within 8.5 arcmin of the NGC 6723 centre, over the PM components (mas yr^{-1}), after the remaining cleaning of the sample. The weighted mean PM and the selection area are shown by the white cross and red circle, respectively.
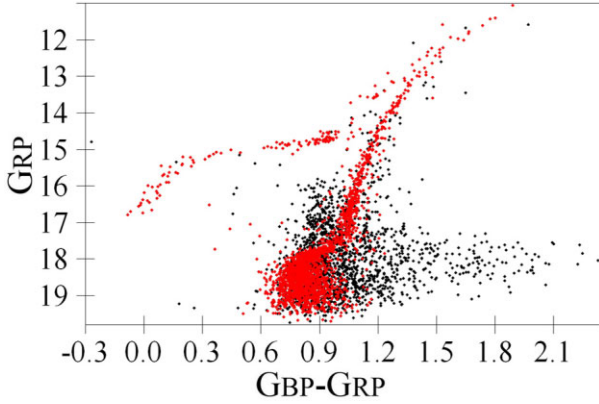

Figure 4. $G_{BP} - G_{RP}$ versus G_{RP} CMD for NGC 6723 stars selected (red symbols) and rejected (black symbols) by their parallaxes and PMs after the remaining cleaning of the sample.

EDR3, but using different approaches. The estimates are consistent within ± 0.01 mas yr^{-1}. However, all these estimates may be equally affected by yet poorly known *Gaia* EDR3 PM systematic errors. VB21 note that such errors impose 'the irreducible systematic floor' on the total accuracy of the *Gaia* EDR3 PMs 'for any compact stellar system'. Such total uncertainty is given in Table 3 for the estimates of VB21, while only the random uncertainty is given for our and Vitral (2021) estimates. We adopt the total uncertainties as the final ones of our PMs.

Similarly, the total uncertainty of *Gaia* EDR3 parallaxes, determined by VB21 as 0.011 mas, is adopted for our median parallaxes of cluster members. After the correction of the parallax zero-point following Lindegren et al. (2021b), we present these median parallaxes in Table 1. We compare these parallaxes with distances, derived in our isochrone fitting, in Section 5.4.

The final lists of the *Gaia* EDR3 cluster members are presented in Table 4.

Table 3. The cluster systemic PMs (mas yr^{-1}). The random uncertainties are presented for the PMs from this study and from Vitral (2021), while the total (random plus systematic) uncertainty is presented for the PMs from VB21.

Cluster	Source	$\mu_\alpha \cos(\delta)$	μ_δ
	This study	-5.512 ± 0.003	-4.780 ± 0.004
NGC 6362	VB21	-5.504 ± 0.024	-4.763 ± 0.024
	Vitral (2021)	-5.509 ± 0.003	-4.763 ± 0.003
	This study	1.021 ± 0.008	-2.427 ± 0.007
NGC 6723	VB21	1.030 ± 0.026	-2.418 ± 0.026
	Vitral (2021)	1.028 ± 0.006	-2.419 ± 0.006

Table 4. The list of the *Gaia* EDR3 members of NGC 6362 and NGC 6723. The complete table is available online.

NGC 6362	NGC 6723
5813076160252430208	6730890124282434688
5813077259764184320	6730890193014007040
5813077264076635648	6730890880196684672
5813077465922524416	6730890880208577280
5813077500282241024	6730890948916284544
...	...

4.3 Cluster members in other data sets

NGC 6362 and NGC 6723 are at middle Galactic latitudes and their fields are moderately contaminated by foreground stars. Therefore, special effort is needed to identify cluster members (except data sets with fiducial sequences only). Nardiello et al. (2018), Piotto et al. (2002), ZKR12, and NKP17 have cleaned their data sets from non-members by use of dedicated PMs. Although imperfect, this membership identification cannot be significantly improved by use of the *Gaia* data. In contrast, we create SMSS, VISTA, and unWISE data sets for our study by cross-identification of our *Gaia* EDR3 cluster members with the SMSS, VISTA, and unWISE catalogues, respectively.

The third group, the data sets of SPZ19 and Lee (2019), can be fitted by isochrones as is. However, we cross-identify our *Gaia* EDR3 cluster members with these data sets and fit isochrones to both the initial data sets and to *Gaia* EDR3 cluster members in these data sets. The *Gaia* membership identification appears to be important, since it not only cleans fiducial sequences but also correct them for a bias due to a non-uniform distribution of non-members in CMDs. Note that Table 2 shows a majority of the SPZ19 and Lee (2019) initial stars lost in this cross-identification with *Gaia*. However, many lost stars are not non-members but stars, which are too faint for *Gaia*. Accordingly, they are rather faint MS stars, that cannot impact our results.

Fig. 5 shows an initial SPZ19 CMD versus the same CMD with the *Gaia* EDR3 cluster members from the SPZ19 data set. It is seen that the *Gaia* EDR3 cluster members are limited to about 2 mag fainter than TO. The initial data set has a lot of contaminants around the HB, above the SGB and redder than the MS. They would bias the best-fitting isochrones and, hence, the derived parameters of the cluster. Use of the initial data set instead of its *Gaia* EDR3 cluster members would increase derived distance by about 50 pc. Age derived from the HB-SGB magnitude difference would decrease by about 0.5 Gyr, while age derived from the SGB length would increase by about 0.5 Gyr. It is seen that the isochrones in Fig. 5 (a) tend to be redder than the contaminated RGB and bluer than the contaminated MS, while they fit the clean RGB and MS in Fig. 5 (b) much better. As a
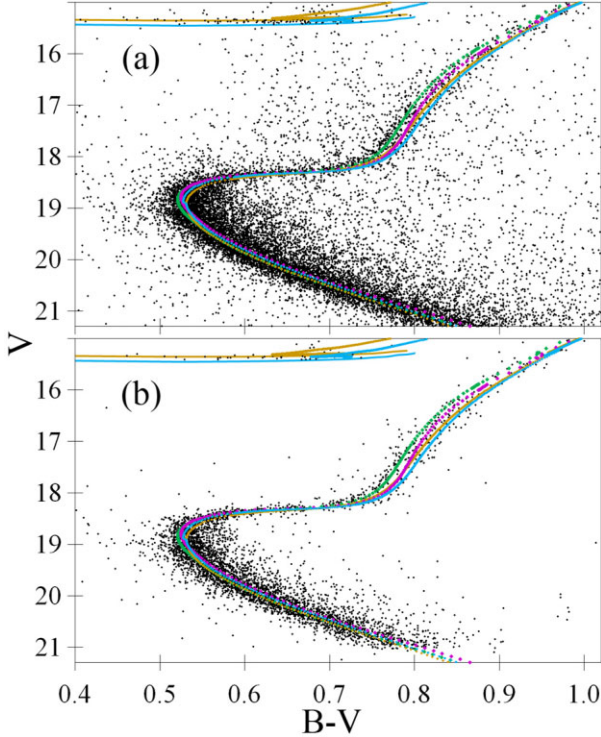
Figure 5. $B - V$ versus V CMDs of NGC 6362 for (a) the initial SPZ19 data set and (b) the *Gaia* EDR3 cluster members from the SPZ19 data set. The isochrones (same for both the charts) from BaSTI for $Y = 0.25$ (blue) and 0.275 (brown) and from DSED for $Y = 0.25$ (purple) and 0.275 (green) are calculated with the best-fitting parameters from Table 6.

Figure 6. A part of the $b - y$ versus V CMD for the data from Lee (2019) for the (a) southern and (b) northern half (in Galactic coordinates) of the NGC 6723 field. The isochrones (same for both the charts) from BaSTI for $Y \approx 0.25$ (blue) and 0.275 (brown) and from DSED for $Y \approx 0.26$ (purple) are calculated with the best-fitting parameters from Table 6. The black arrow shows reddening and extinction corresponding to $E(B - V) = 0.1$ mag.

result, contaminants would decrease/increase the reddening derived for the RGB/MS, respectively, by few hundredths of a magnitude. Thus, contaminants introduce a discrepancy between the cluster parameters derived from different domains of CMD. Hence, the final results from contaminated data would depend on our preferences to use one domain or another. Finally, hereafter, we use only the *Gaia* EDR3 cluster members from the SPZ19 and Lee (2019) data sets instead of the initial data sets. The expense is that we lose the faint MS stars and almost all stars within a central arcminute of the clusters.

An example of a bias of a derived parameter due to a contamination of a CMD is the Alcaino et al. (1999) data set. We do not have its star-by-star photometry, but only its fiducial sequences. Hence, we cannot cross-identify it and eliminate non-members. A strong non-member contamination of the MS is seen in Alcaino et al. (1999)'s figures. As a result, the median $B - V$ TO colour of the Alcaino et al. (1999) data set is about 0.04 mag redder than that of SPZ19 data set. Therefore, we decided to reject the Alcaino et al. (1999) data set.

Fig. 5 shows a segregation of the RGB into two populations. The redder population is better fitted by the BaSTI isochrone with $Y = 0.25$ (though the DSED isochrone with $Y = 0.25$ is also acceptable), while the bluer population – by the DSED isochrone with $Y = 0.275$. This suggests a helium abundance difference $\Delta Y \approx 0.025$ between the populations, in line with its estimates in Section 2. Note that the colour difference between the BaSTI isochrones with $Y = 0.25$ and 0.275 is much lower than that between the observed segregated RGBs. However, the observed segregated AGBs are well reproduced by these BaSTI isochrones.
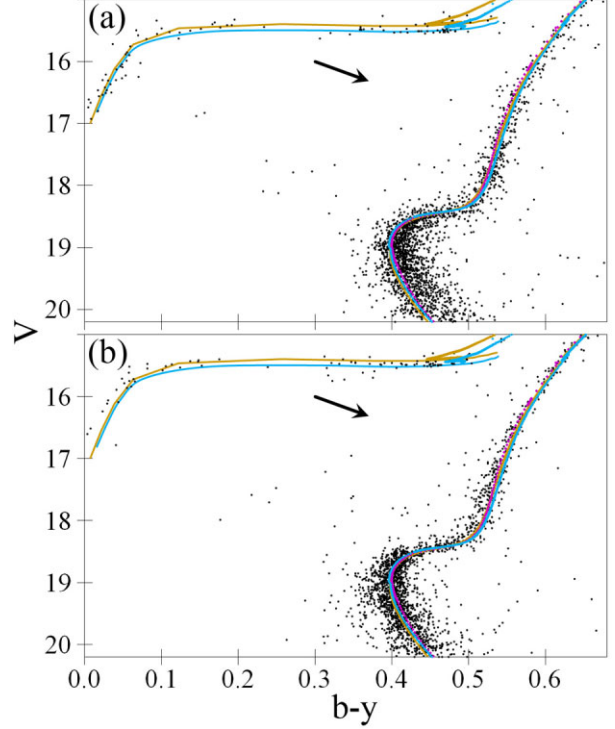
4.4 Differential reddening

The differential reddening in the field of NGC 6723 forces us to correct it for all data sets, except HSV12 and Piotto et al. (2002). Fortunately, the differential reddening in the NGC 6723 field increases along Galactic latitude, since its apparent source, the Corona Australis cloud complex, is located south of NGC 6723 (in Galactic coordinates). SFD98 and our CMDs confirm a differential reddening gradient with latitude. Two examples of such CMDs are shown in Figs 6 and 7. Stars of the southern and northern (in Galactic coordinates) halves of the NGC 6723 field tend to be on the opposite sides of the same reference isochrones, though the southern stars show a larger deviation and scatter. The reddening vector indicates that the southern stars are shifted w.r.t. the northern ones by a higher reddening of the order of $E(B - V) \approx 0.1$ mag. This effect is the same for all CMD domains.

We calculate differential reddening as a function of latitude using the approach applied in Paper II and Paper III. Namely, some partial fiducial sequences for several latitude bins are analysed. Only the large data sets of Nardiello et al. (2018), *Gaia* EDR3, SPZ19, and Lee (2019) have enough stars to consider differential reddening in many latitude bins. For comparison, the obtained differential reddenings are set to zero at the cluster centre and converted into $\Delta E(B - V)$ by use of the Cardelli, Clayton & Mathis (1989, hereafter CCM89) extinction law with extinction-to-reddening ratio $R_V \equiv A_V/E(B - V) = 3.1$. Fig. 8 shows the differential reddening in the field of NGC 6723 as a function of Galactic latitude for the data sets of Lee (2019) ($b - y$ versus V CMD), SPZ19 ($B - V$ versus V and $V - I$ versus I CMDs), and Nardiello et al. (2018) ($F606W$–$F814W$
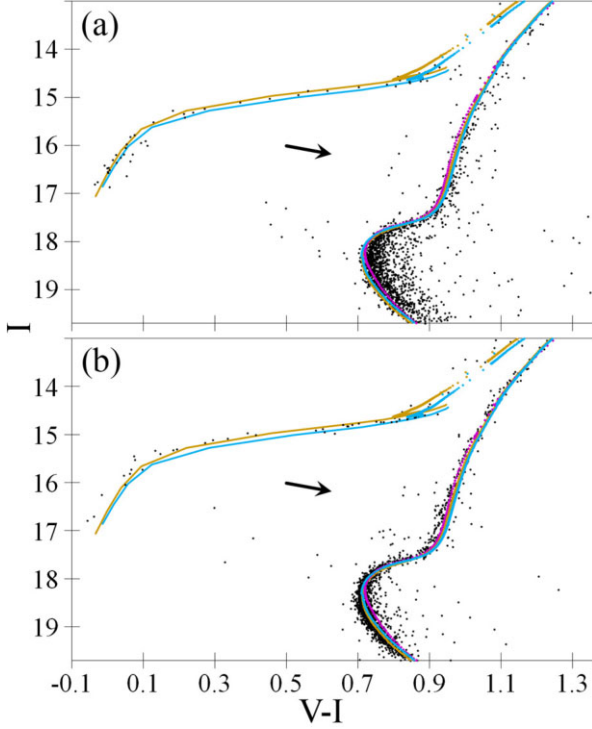
Figure 7. The same as Fig. 6 but for $V - I$ versus I CMD for the *Gaia* EDR3 cluster members among the SPZ19 data set for NGC 6723.
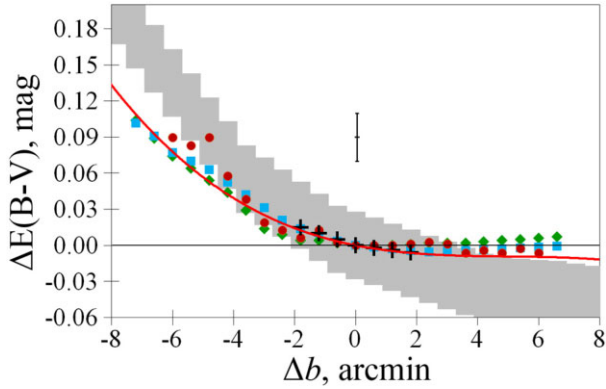

Figure 8. Differential reddening $\Delta E(B - V)$ in the field of NGC 6723 as a function of Galactic latitude Δb w.r.t. the cluster centre: derived from the $b - y$ versus V CMD (Lee 2019) – brown circles, $B - V$ versus V CMD (SPZ19) – green diamonds, $V - I$ versus I CMD (SPZ19) – blue squares, and *HST* F606W–F814W versus F814W CMD (Nardiello et al. 2018) – black crosses by use of CCM89 extinction law with $R_V = 3.1$. The uncertainty of ± 0.02 mag for these results is shown by the separate error bar. The differential reddening from SFD98 with its stated precision ± 0.028 mag is shown by the grey area. The approximating equation (1) is shown by the red curve.

versus F814W CMD). Also, the differential reddening from SFD98 is shown by the grey area. Good agreement between all data sets is observed.

Note that the *HST* data set of Nardiello et al. (2018) covers only a central area of 3.4×3.4 arcmin and, accordingly, shows a differential reddening corresponding to only $\Delta E(B - V) = 0.02$ mag over the area. Such negligible differential reddening must appear for any data
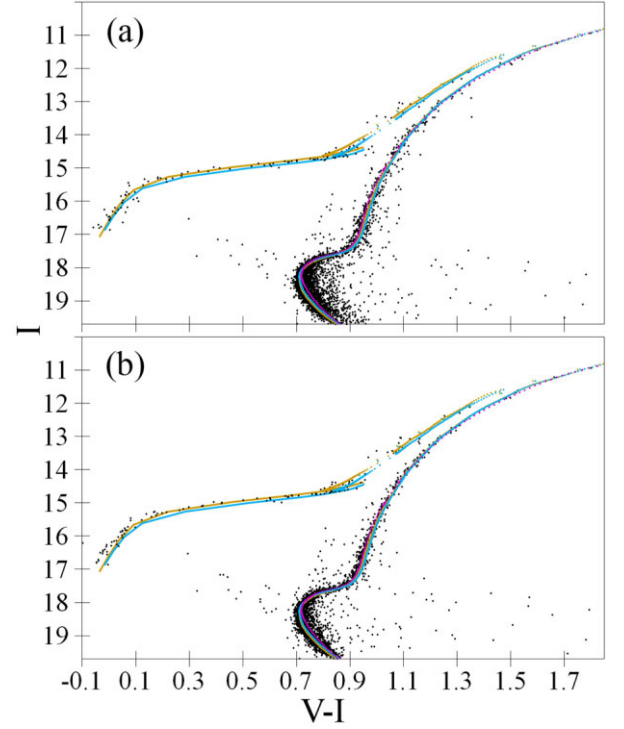

Figure 9. The same as Fig. 7 but for the whole NGC 6723 field (a) before and (b) after the correction for differential reddening.

set covering only a central part of the field.[18] This may explain why such a strong differential reddening at the periphery was not recognized earlier.

A deviation of the data sets from the SFD98 in Fig. 8 can be explained by (i) systematic variations of the cluster stellar content with its radius or (ii) SFD98 calibration errors. Either way, we assume a decrease of reddening to the North across the whole cluster field. Therefore, we approximate the differential reddening by a third-order polynomial taking into account the differential reddening results from all the large data sets:

$$\Delta E(B - V) = -13.6750\Delta b^3 + 3.5958\Delta b^2 - 0.30\Delta b, \qquad (1)$$

where Δb is the latitude offset in degrees w.r.t. the cluster centre. This polynomial is shown in Fig. 8 by the red curve. This suggests a differential reddening up to $\Delta E(B - V) \approx 0.13$ mag at the Southern periphery of the NGC 6723 field.

We use equation (1) to correct the differential reddening in all the data sets, except HSV12 and Piotto et al. (2002). This procedure reduces the scatter of the photometric data around the fiducial sequences. An example is given in Fig. 9 where the CMD from Fig. 7 is shown for the whole NGC 6723 field (a) before and (b) after the correction for differential reddening.

All reddening estimates for NGC 6723, obtained in our isochrone fitting of CMDs, are referred to the cluster centre, where reddening and extinction are rather low. Hence, these are not estimates of an average or median reddening in the NGC 6723 field. Therefore, to estimate reddening in a part of the NGC 6723 field, one should estimate differential reddening in this part by use of equation (1) and add it to our reddening estimate for the cluster centre.

---

[18]To our knowledge, this applies to the HSV12 and Piotto et al. (2002) data sets.

Table 5. The fiducial sequences for NGC 6362 and NGC 6723 G_{RP} versus $G_{BP} - G_{RP}$ based on the data of *Gaia* EDR3. The complete table is available online.

NGC 6362		NGC 6723	
RP	BP − RP	RP	BP − RP
15.48	0.12	16.75	− 0.07
15.40	0.14	16.50	− 0.02
15.34	0.16	15.94	0.07
15.24	0.20	15.67	0.13
15.20	0.22	15.40	0.20
...	...	...	...

4.5 Fiducial sequences

In order to fit data by a theoretical isochrone, we present them by a fiducial sequence, i.e. a colour–magnitude relation for single stars. We calculate such a sequence as a locus of the number density maxima in some colour–magnitude bins. Some details and examples are given in section 3 of Paper II.

The HB, AGB, bright RGB and sometimes other CMD domains contain a small number of stars. In such a case, a fiducial point is defined by a few or even just one star with rather precise photometry, i.e. if a colour and magnitude of such fiducial point/points can be defined within ±0.04 mag. The balance of uncertainties, presented in appendix A of Paper II, shows that such an uncertainty of a fiducial point is negligible w.r.t. total uncertainty, since we use a lot of fiducial points to derive [Fe/H], distance, age, and reddening.

The fiducial sequences for the *Gaia* EDR3 data sets are presented in Table 5 as an example. All other fiducial sequences can be provided on request.

We find that the populations are segregated at the HB in almost all CMDs, at the AGB in CMDs with a considerable number of the AGB stars, as well as at the RGB in some CMDs (an example is gives in Fig. 5). We find no CMD for these GCs with the populations segregated at the SGB, TO, or MS.

In the case of no segregation, an unresolved mix of the populations is presented by a fiducial sequence, which, in turn, is fitted by an interpolated isochrone with $Y = 0.26$, as noted in Section 3. In the case of segregation, each population is presented by its own fiducial sequence, which, in turn, is fitted by its own primordial or helium-enriched isochrone of the same model, [Fe/H], distance, reddening, and age. However, in some cases, we cannot fit a population by an isochrone with a reasonable abundance.

To derive the best-fitting parameters from a CMD, we select an isochrone with a minimal total offset between the isochrone points and the fiducial points in the same magnitude range of the CMD.

Fig. 10 shows an example of isochrones fitting fiducial sequences, which, in turn, are constructed for bulks of stars. This figure combines two CMDs for the twin SPZ19 data sets. All nine CMDs of the twin data sets provide a similar gauge, since they show similar results (see Table 6). When comparing two clusters, we present this as the Hertzsprung–Russell diagrams created from related CMDs (one of which is presented in Fig. 5) by use of reddening, extinction, and distance estimates from Table 6 and the same [Fe/H] = −1.05. It is worth noting that a good fitting of the fiducial points by the isochrones in Fig. 10, when the HB and RGB of two clusters coincide, indicates that we use correct reddenings, extinctions, and distances for both the clusters.

Example areas across the TO and RGB are shown by the black boxes in Fig. 10. Their profiles are given in Fig. 11. A median colour can be easily derived from the TO profiles. In contrast, the RGB
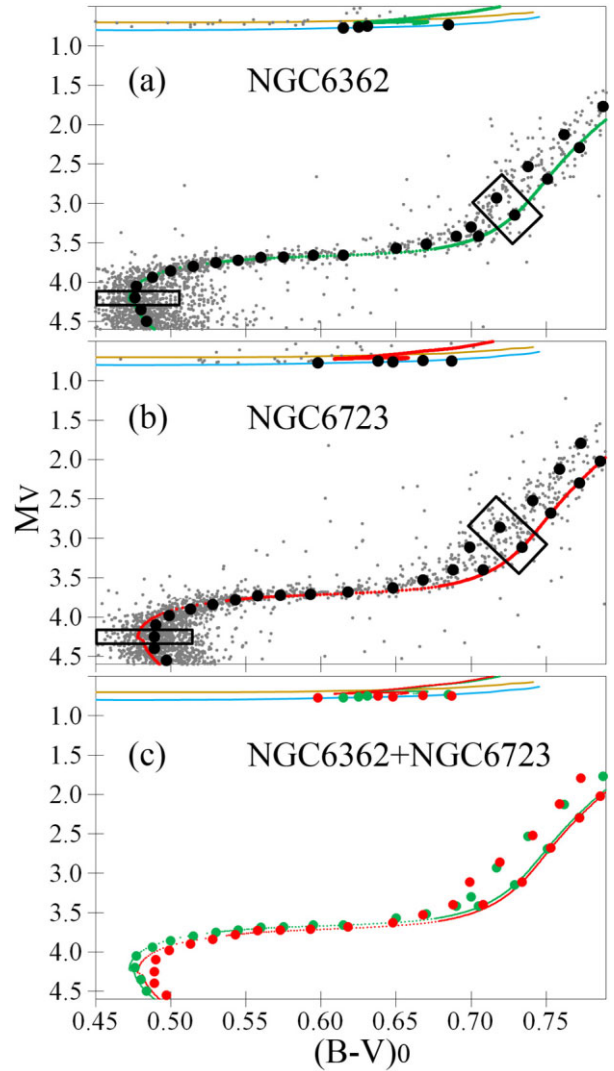

Figure 10. Hertzsprung–Russell diagram $(B − V)_0$ versus M_V for NGC 6362 and NGC 6723 with the *Gaia* EDR3 members of the SPZ19 data sets: stars – grey dots, fiducial points – black circles (green and red in the bottom plot for NGC 6362 and NGC 6723, respectively), best-fitting BaSTI ZAHB for [Fe/H] = −1.05 and $Y = 0.25$ – blue curve, best-fitting BaSTI ZAHB for [Fe/H] = −1.05 and $Y = 0.275$ – brown curve, NGC 6362 best-fitting BaSTI isochrone for [Fe/H] = −1.05, $Y = 0.25$ and age 12 Gyr – green curve, NGC 6723 best-fitting BaSTI isochrone for [Fe/H] = −1.05, $Y = 0.25$ and age 12.5 Gyr – red curve. All the data are corrected for reddening, extinction, and distance estimates from Table 6. Black boxes show the cross sections from Fig. 11.

profiles show the segregation of stars, discussed in Section 4.3 and seen in Fig. 5. The bluer population (presumably helium-enriched) dominates. However, the stars counts allow us to set fiducial sequence points with a precision of a hundredth of a magnitude for colour and about 0.1 – for magnitude, as seen in Fig. 10.

Fig. 10 shows that each HB fiducial point is defined by only one star. Yet, the *Gaia* membership cross-identification (see Section 4.3) ensures us that such a star is a cluster member. HB stars magnitude better defines distance modulus of clusters. Rather bright HB stars in the SPZ19 data sets have a magnitude uncertainty of about 0.01 mag. Therefore, even a few engaged HB stars provide us with a statistical uncertainty of an average or median HB magnitude of better than 0.01 mag, i.e. much better than a systematic uncertainty of about 0.04 mag (see Section 3.1). Note that the HB stars, which are bluer

Table 6. The results of the isochrone fitting for various models and some key CMDs for both the clusters. In all the CMDs, the colour is the abscissa and the magnitude in the redder filter is the ordinate, except the Lee (2019) CMD where $b - y$ is the abscissa and V is the ordinate. The NGC 6723 reddenings are referred to the cluster centre. The derived reddenings are converted to $E(B - V)$, given in parentheses, by use of extinction coefficients from Casagrande & VandenBerg (2014, 2018a,b). The complete table is available online.

CMD colour	NGC 6362		NGC 6723	
	DSED	BaSTI	DSED	BaSTI
$E(F606W–F814W)$ *HST* ACS	0.074 ± 0.02 (0.08)	0.058 ± 0.02 (0.06)	0.079 ± 0.03 (0.08)	0.060 ± 0.03 (0.06)
$F606W–F814W$ age, Gyr	12.5	12.5	12.5	13.0
$F606W–F814W$ distance, kpc	7.7	7.7	8.2	8.1
$F606W–F814W$ [Fe/H]	-1.10	-1.00	-1.15	-1.00
$E(G_{BP} - G_{RP})$ EDR3	0.132 ± 0.03 (0.10)	0.093 ± 0.03 (0.07)	0.126 ± 0.03 (0.10)	0.097 ± 0.03 (0.07)
$G_{BP} - G_{RP}$ age, Gyr	12.5	12.5	13.0	13.0
$G_{BP} - G_{RP}$ distance, kpc	7.6	7.5	8.1	8.1
$G_{BP} - G_{RP}$ [Fe/H]	-1.15	-1.00	-1.15	-1.05
$E(B - V)$ SPZ19	0.071 ± 0.03 (0.07)	0.053 ± 0.03 (0.05)	0.085 ± 0.03 (0.09)	0.060 ± 0.03 (0.06)
$B - V$ age, Gyr	11.5	12.0	12.5	12.5
$B - V$ distance, kpc	7.8	7.8	7.9	8.1
$B - V$ [Fe/H]	-1.10	-1.05	-1.15	-1.05
$E(g - r)$ SkyMapper DR3	0.047 ± 0.02 (0.07)	0.040 ± 0.02 (0.06)	0.059 ± 0.03 (0.08)	0.048 ± 0.03 (0.07)
$g - r$ age, Gyr	12.0	12.0	12.0	12.5
$g - r$ distance, kpc	7.7	7.7	8.3	8.2
$g - r$ [Fe/H]	-1.10	-1.00	-1.15	-1.05
$E(F439W–F555W)$ *HST* WFPC2	0.056 ± 0.03 (0.05)	0.041 ± 0.03 (0.04)	0.067 ± 0.03 (0.07)	0.046 ± 0.03 (0.04)
$F439W–F555W$ age, Gyr	12.5	12.0	12.0	12.5
$F439W–F555W$ distance, kpc	7.9	8.1	8.6	8.5
$F439W–F555W$ [Fe/H]	-1.10	-1.05	-1.15	-1.05
...	...	...	...	...

than those marked by the fiducial points in Fig. 10, can be RR Lyrae variables or can belong to a helium-enriched population and, hence, must be fitted by a helium-enriched isochrone (e.g. that with $Y = 0.275$ in Fig. 10).

Similar to the HB, the SGB magnitude and the HB–SGB magnitude difference can be determined with a random precision of about 0.01 mag and systematic accuracy of few hundredths of a magnitude. The HB–SGB magnitude difference better defines cluster age. The high precision of the *Gaia*–SPZ19 data sets allows one to see in Fig. 10(c) that the SGB of NGC 6362 is about 0.04 mag brighter than that of NGC 6723. This means that the former is slightly younger than the latter: the best-fitting isochrones in Fig. 10(c) differ by 0.5 Gyr. It would seem that the magnitude difference of 0.04 mag can easily get lost in the systematic uncertainties of 0.04 for both the HB and SGB magnitudes. Moreover, the situation in Fig. 10 (c) is further aggravated by the segregation of the faint RGB. However, the systematic uncertainties must be the same for both clusters and, hence, are canceled in relative estimates. Yet, an age difference of about 0.5 Gyr may be the sensitivity limit for such an isochrone fitting with the best current data sets and models.

Age is also defined by the length of the SGB between the TO and RGB. Fig. 10(c) shows that NGC 6362 has a longer SGB and, hence, is younger. Thus, two proxies of age agree in this case. However, the length of the SGB may be affected by significant systematics from stellar modeling. This appears to be a bad fit of the TO when the HB and RGB of two clusters coincide. This is seen for NGC 6723 in Fig. 10(c).

5 RESULTS

With this wealth of photometric data, we fit isochrones to dozens of CMDs with different colours. As in our previous papers, results for adjacent CMDs are consistent within their precision: e.g. results for

a CMD with the $B - I$ colour are consistent with those for CMDs with the $B - V$, $V - R$, and $R - I$ colours. Hence, we show only some examples of the CMDs with isochrone fits in Figs 9 and 12. Some more examples are given in Appendix A. Figures for all the CMDs can be provided on request. The derived [Fe/H], ages, distances, and reddenings for the most important CMDs are presented in Table 6. For comparison, the derived reddenings are converted to $E(B - V)$, given in parentheses, by use of extinction coefficients from Casagrande & VandenBerg (2014, 2018a,b).

For most CMDs, the isochrone-to-fiducial fitting is so precise that the best-fitting isochrones of the models almost coincide with each other and with our fiducial sequence on the scales of our CMD figures for the RGB, SGB, and TO. Hence, usually we do not show our fiducial sequences for clarity.

The predicted statistic uncertainties of the fitting are similar to those described in the balance of uncertainties, presented in appendix A of Paper II. For each combination of a fiducial sequence and its best-fitting isochrone, we find the maximal offset of this isochrone w.r.t. this fiducial sequence along the reddening vector (i.e. nearly along the colour). Such an offset is given in Table 6 after each value of reddening as its empirical uncertainty. Usually, the predicted and empirical uncertainties are comparable. The largest value in such a pair of the uncertainties is shown by error bars in Figs 14 and 15, which demonstrate our resulting extinction laws. However, it is worth noting that systematic uncertainties of isochrones always dominate in final uncertainty (see Section 3.1).

For example, let us consider the uncertainty of [Fe/H] derived from the slope of the RGB. Taking into account RGB geometry, the number of stars used, their photometric precision, and slope sensitivity to variations of [Fe/H], we predict a random uncertainty of [Fe/H], derived from a pair of a CMD and a model, as of about 0.15 dex. Eleven (NGC 6362) or ten (NGC 6723) CMDs, used for our final average [Fe/H] estimate, might provide their uncertainty of
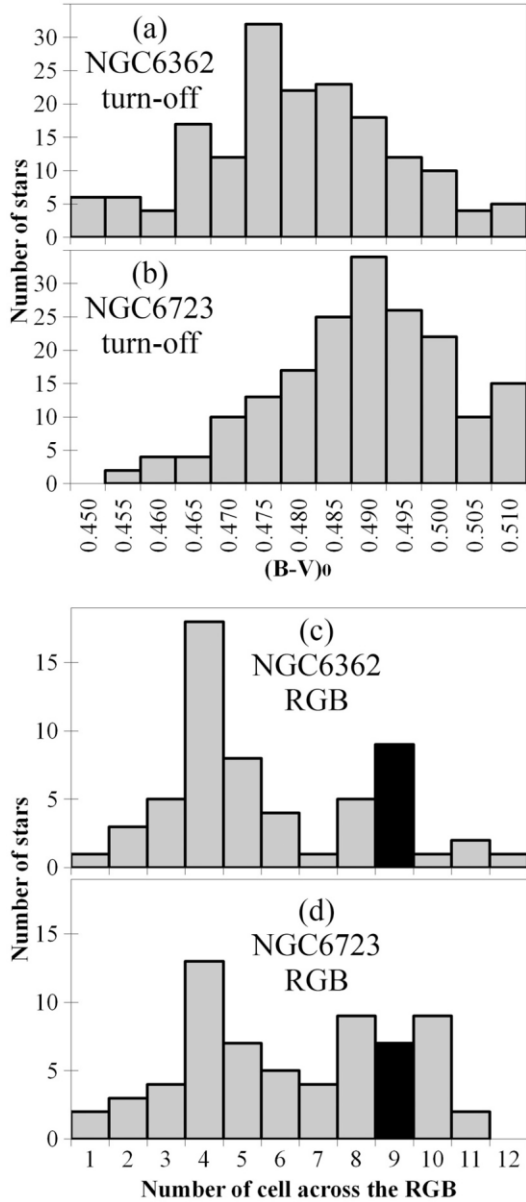
Figure 11. The distribution of the TO stars along $(B - V)_0$ and RGB stars across the RGB inside the boxes from Fig. 10. The black bars mark the positions of the RGB fiducial sequence points.

about 0.05 dex by use of a model. However, the models may show a systematic difference between their average [Fe/H] estimates larger than 0.05 dex.

5.1 Issues

The VISTA photometry strongly deviates blueward from the isochrones for the bright RGB ($J_{VISTA} < 12$ and <13 for NGC 6362 and NGC 6723, respectively). It seems to be an error in the VISTA photometry for very bright stars. However, the remaining VISTA stars are enough to derive accurate parameters.

Generally, an UV, UV–optical, optical–IR, and IR–IR CMD contains less stars, more contaminants, and less populated HB, TO, and MS than a typical optical CMD. Moreover, isochrones are less accurate for such CMDs. In addition, *HST* WFC3 UV filters are sensitive to the CNO abundances through OH, CN, NH, and CH
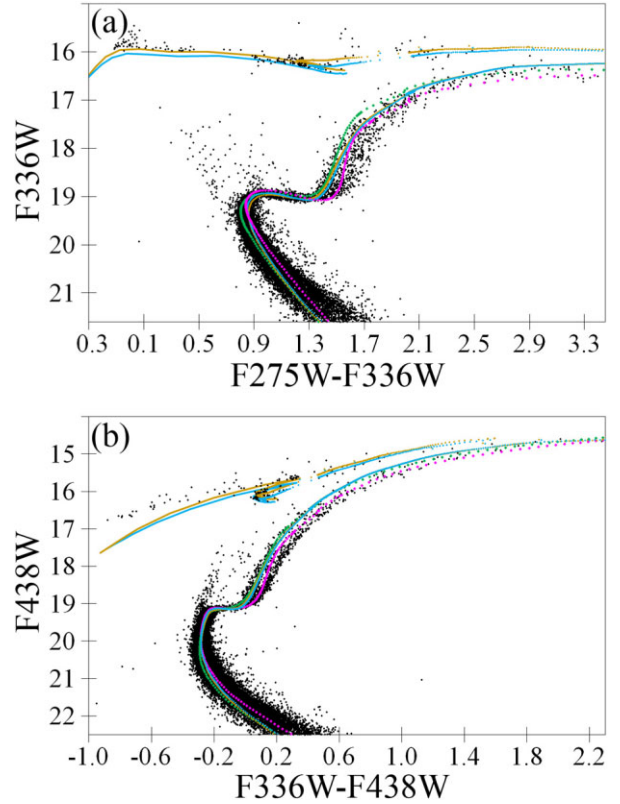

Figure 12. The UV CMDs for NGC 6723 with the (a) *F275W–F336W* and (b) *F336W–F438W* colours. The isochrones from BaSTI for $Y \approx 0.25$ (blue) and 0.275 (brown) and from DSED for $Y \approx 0.25$ (purple) and 0.33 (green) are calculated with the best-fitting parameters from Table 6.

bands (VandenBerg et al. 2022). However, some of such CMDs provide reliable [Fe/H], distance, age, and reddening estimates (see Table 6). Examples, given in Fig. 12, show that almost all UV CMD domains are fitted by the isochrones rather successfully, i.e. with reasonable residuals and reliable fitting parameters (see Table 6). Similarly for both the CMDs, the worst fitting is found for the middle RGB (within 0.1 mag in colour) and blue HB (up to 0.8 mag for the *F438W* magnitude). However, both DSED and BaSTI cannot explain the segregation of the RGB populations by a reliable $\Delta Y = 0.025$. Only the DSED isochrones with a very large $\Delta Y = 0.08$ can do it.

Anyway, we do not use the results from UV, UV–optical, optical–IR, and IR–IR pairs (including those presented in Table 6) for our final results, except the reddening $E(V - J_{2MASS})$ derived for the HSV12 data set and used for our final reddening estimate. Fig. 15 shows that $E(V - J_{2MASS})$ (open red circle) agrees with other results.

Another example of an issue in the UV is the U photometry for NGC 6723 (but not for NGC 6362). Both the independent data sets with it, Alcaino et al. (1999) and SPZ19, are consitent in their unreliable U magnitudes: they should be about 0.12 mag fainter. Otherwise, a large negative reddening $E(U - B)$ is derived in the isochrone fitting. Thus, we reject the U filter for NGC 6723 from our consideration.

HST WFC3 *F438W* and ACS *F606W* filters would be a valuable proxy for the B and V filters. However, belonging to the different detectors (WFC3 and ACS), these filters may allow a small instrumental systematic error in the *F438W–F606W* colour. Indeed, Figs 14 and 15 show a fracture of the *HST* empirical extinction laws (red diamonds) between the *F438W* and *F606W* filters. This fracture seems to be

similar for BaSTI and DSEP. This forces us to exclude the WFC3 filters for our final estimates of [Fe/H], age, distance, and reddening.

For NGC 6362, the ZKR12, NKP17, and SPZ19 data sets provide photometry in the B and V filters. We cross-identify these data sets for a direct comparison and discover their magnitude differences to be up to 0.04 mag as some functions of magnitude. However, these functions are rather correlated for B and V, providing only small systematic differences within 0.02 mag between their $B - V$ colours. Such magnitude and colour differences at a level of few hundredths of a magnitude are common and expected (SPZ19). Comparing the descriptions of these three data sets, we conclude that the reason for these inconsistencies is unknown. However, we lack justification to exclude any of these data sets. Therefore, we process and fit them as is. The resulting parameters of the three data sets are similar, as seen in Table 6. Also, the similarity of their extinctions is seen from Fig. 14. Therefore, we use all three data sets for our final results.

In order to see all systematic differences between the data sets in Figs 14 and 15, we do not adjust the data sets with similar filters, in contrast to Paper II and Paper III.

5.2 HB

In our CMDs, we show both the primordial and helium-enriched HB isochrones for the whole colour range covered by the HB stars in order to show that the primordial and helium-enriched populations dominate the red and blue HB, respectively, in accordance with Mucciarelli et al. (2016) and Heber (2016).

Our fitting of the observed colour distribution of the HB stars by the BaSTI extended HB set allows us to estimate the mass range for the majority of the HB stars (separately for the populations): 0.62–0.70 and 0.58–0.61 $M_\odot$ for the primordial and helium-enriched populations of NGC 6362, respectively; 0.63–0.70 and 0.55–0.61 $M_\odot$ for the primordial and helium-enriched populations of NGC 6723, respectively. These estimates are obtained consistently for all CMDs, which are rich in HB stars. Yet, these estimates may be uncertain due to the incompleteness of our HB samples and ambiguity regarding the population to which some stars belong. However, these estimates can be compared with those from Tailo et al. (2020), who combine *HST* photometry and stellar population models to infer the average HB masses. They obtain 0.64 ± 0.03 and $0.60 \pm 0.03\,M_\odot$ for the primordial and helium-enriched populations of NGC 6362, respectively, and 0.65 ± 0.02 and $0.56 \pm 0.02\,M_\odot$ for the primordial and helium-enriched populations of NGC 6723, respectively. Since we use different theoretical models from Tailo et al. (2020), a good agreement of these results is remarkable.

5.3 Metallicity

An example of the RGB slope fitting is presented in Fig. 13. This shows the Hertzsprung–Russell diagram for the *Gaia* EDR3 members of the SPZ19 data sets in both clusters. All the data are corrected for reddening, extinction, and distance estimates from Table 6. The RGBs are fitted by isochrones with different [Fe/H] and ages. Helium primordial and helium-enriched isochrones are shown for the HBs and RGBs, respectively, following our suggestions about their helium abundance in these clusters (although the blue HB, out of this figure, is helium-enriched).

By use of 11 independent optical CMDs with the well-populated RGB, we estimate the average [Fe/H] = -1.10 and -0.97 for NGC 6362 by use of DSED and BaSTI, respectively. We adopt their mean [Fe/H] = -1.04 ± 0.07 (with uncertainty as half the
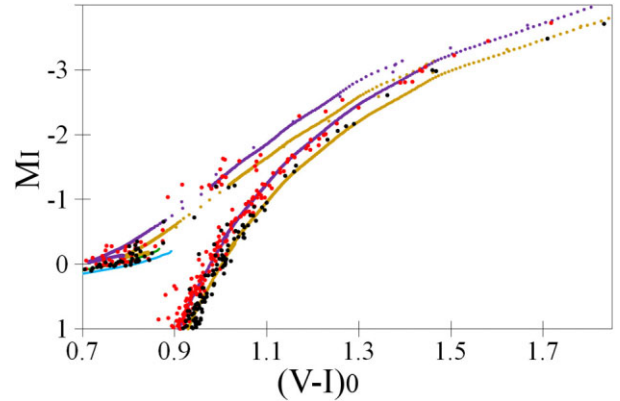

Figure 13. Hertzsprung–Russell diagram $(V - I)_0$ versus M_I for NGC 6362 and NGC 6723 with the *Gaia* EDR3 members of the SPZ19 data sets: NGC 6362 stars (black dots) are fitted by the best-fitting BaSTI isochrone for [Fe/H] = -0.9, $Y = 0.275$ and age 12 Gyr (brown curve) and by the best-fitting BaSTI ZAHB for [Fe/H] = -0.9 and $Y = 0.25$ (blue curve), NGC 6723 stars (red dots) are fitted by the best-fitting BaSTI isochrone for [Fe/H] = -1.05, $Y = 0.275$ and age 12.5 Gyr (purple curve) and by the best-fitting BaSTI ZAHB for [Fe/H] = -1.05 and $Y = 0.25$ (green curve). All the data are corrected for reddening, extinction, and distance estimates from Table 6.

difference between BaSTI and DSED) as our final [Fe/H] estimate for NGC 6362 and use it for CMDs with a sparsely populated RGB.

Similarly, by use of 10 independent optical CMDs with the well-populated RGB, we estimate the average [Fe/H] = -1.15 and -1.04 for NGC 6723 by use of DSED and BaSTI, respectively, and adopt their mean [Fe/H] = -1.09 ± 0.06 as our final [Fe/H] estimate for NGC 6723.

Our [Fe/H] estimates adequately agree with those from Dotter et al. (2010) obtained in their fitting of the same *HST* ACS and WFPC2 photometry by DSED isochrones: [Fe/H] = -1.1 for NGC 6362 and [Fe/H] = -1.0 for NGC 6723.

Kerber et al. (2018) fit the HB, RGB, SGB, and MS of NGC 6362 in a CMD with other *HST* data by use of the BaSTI and DSED isochrones. They obtain [Fe/H] = -1.15 ± 0.08 both for BaSTI and DSED in agreement with our results.

Our [Fe/H] estimates agree with those from Valcin et al. (2020), obtained from isochrone fitting of the *HST* ACS data by DSED: [Fe/H] = $-1.11^{+0.14}_{-0.11}$ and $-1.06^{+0.07}_{-0.15}$ for NGC 6362 and NGC 6723, respectively.

It is important to compare our [Fe/H] estimates with those from spectroscopy. For NGC 6362, there is good agreement within σ with [Fe/H] = -1.09 ± 0.01 from Mucciarelli et al. (2016) and -1.07 ± 0.01 from Massari et al. (2017). For NGC 6723, there is good agreement within σ with [Fe/H] = -1.22 ± 0.08 from Gratton et al. (2015) and [Fe/H] = -0.98 ± 0.08 from Rojas-Arriagada et al. (2016). However, the estimate [Fe/H] = -0.93 ± 0.05 from Crestani et al. (2019) is less consistent with ours, i.e. at a level of 1.5σ.

Cluster RR Lyrae stars with accurately measured properties constrain cluster metallicity and some other parameters. For RR Lyrae stars in NGC 6362, Arellano Ferro et al. (2018) obtain [Fe/H] = -1.066 ± 0.126, $E(B - V) = 0.063 \pm 0.024$, and distance modulus $(m - M)_V = 14.69 \pm 0.08$ from time-series photometry of the RRab stars, with similar results for the RRc stars. These results perfectly agree with ours. Alternative consideration of the same data by VandenBerg & Denissenkov (2018) provides a similar [Fe/H] within its uncertainties. For RR Lyrae stars in NGC 6723, Lee et al. (2014) obtain [Fe/H] = -1.23 ± 0.11, $E(B - V) = 0.061 \pm 0.014$, distance
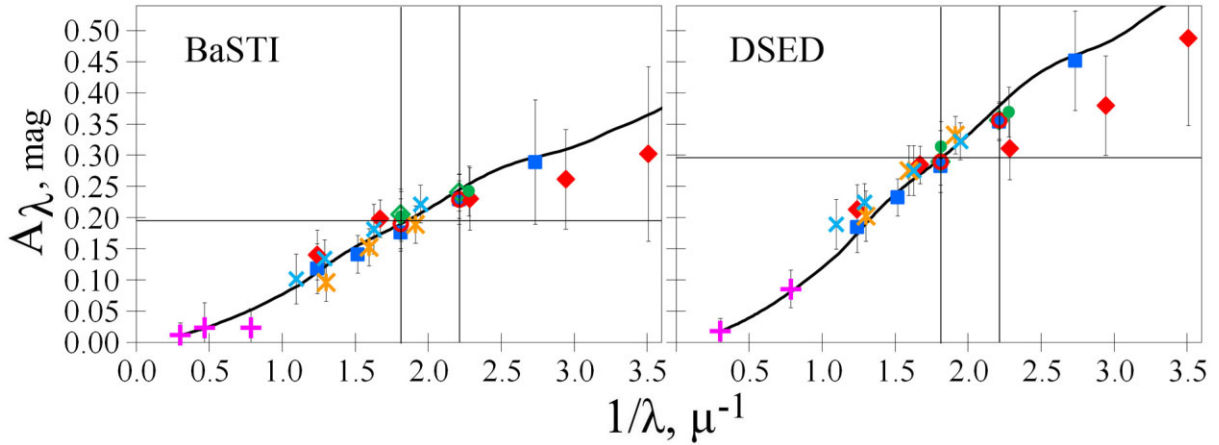
Figure 14. The empirical extinction laws for NGC 6362 from the isochrone fitting by the different models. The data sets are: *HST* ACS and WFC3 by Nardiello et al. (2018) – red diamonds; *HST* WFPC2 by Piotto et al. (2002) – green circles; *Gaia* – yellow snowflakes; SPZ19 – blue squares; SMSS – blue inclined crosses; ZKR12 – open green diamonds; NKP17 – open red circles; IR data sets by VISTA and unWISE – purple upright crosses. The effective wavelengths of the *B* and *V* filters are denoted by the vertical lines. The black curve shows the extinction law of CCM89 with $R_V = 3.1$ with the derived A_V, which is shown by the horizontal line.
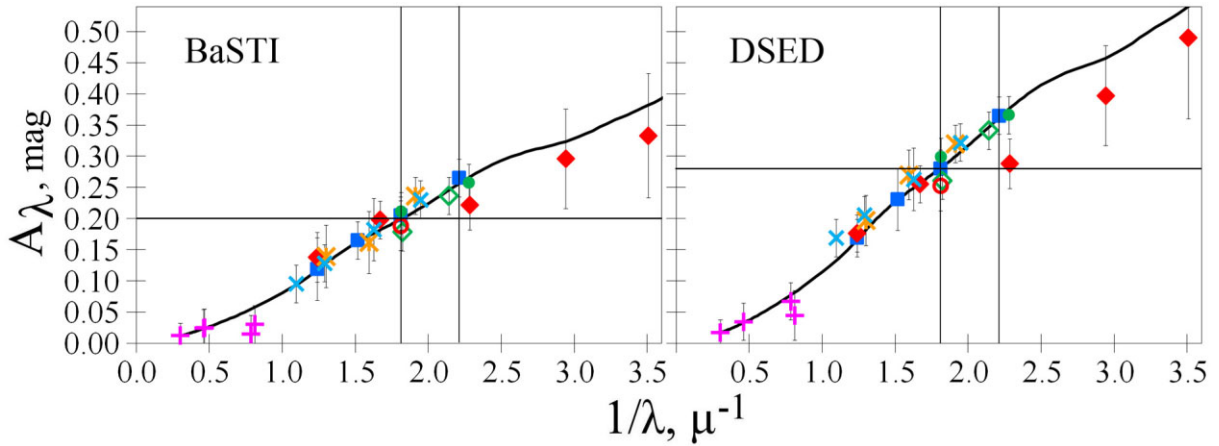

Figure 15. The same as Fig. 14 but for NGC 6723. The data sets are: *HST* ACS and WFC3 Nardiello et al. (2018) – red diamonds; *HST* WFPC2 by Piotto et al. (2002) – green circles; *Gaia* – yellow snowflakes; SPZ19 – blue squares; SMSS – blue inclined crosses; Lee (2019) – open green diamonds; HSV12 (*V* filter) – open red circle; IR data sets by HSV12 (J_{2MASS} and Ks_{2MASS} filters), VISTA, and unWISE – purple upright crosses. The effective wavelengths of the *B* and *V* filters are denoted by the vertical lines. The black curve shows the extinction law of CCM89 with $R_V = 3.1$ with the derived A_V, which is shown by the horizontal line.

modulus 14.65 ± 0.05, equivalent to a distance 8.47 ± 0.17 kpc. All these findings agree with ours.

Photometric and spectroscopic observations of detached eclipsing binaries allow one to derive the masses, radii, and luminosities of their component stars. The obtained mass–radius, mass–luminosity, and colour–magnitude relations can be compared with isochrone predictions to verify [Fe/H], abundance, and age of a cluster containing such binaries. For two eclipsing binaries in NGC 6362, Kaluzhny et al. (2015) obtained reliable results with fitting by DSED, assuming [Fe/H] $= -1.07$. They verified that a change from [Fe/H] $= -1.07$ to -1.15 'does not influence the parameters of the binaries in any significant way'. However, both the components of a binary provide a good isochrone fitting only (i) if their ages differ by 1.5 ± 0.7 Gyr (Kaluzhny et al. 2015) or (ii) if their helium abundances differ by about $\Delta Y \approx 0.02$ (VandenBerg & Denissenkov 2018), or (iii) if the binary has a higher C, N, and O abundance than in stellar models used (VandenBerg et al. 2022). These conditions are possible, since they do not contradict the known properties of NGC 6362.

5.4 Distance and age

Similar to our previous papers, the derived distances and ages for the optical range (filters with their effective wavelengths within $400 < \lambda_{eff} < 1000$ nm except *HST* WFC3 *F438W*) differ from those for the UV and IR ranges, both systematically and by their standard deviations. The optical CMDs are preferable in terms of star quantity, sample completeness, photometric accuracy, and systematic accuracy of the models. Therefore, we use the distance and age estimates in the optical range for our final estimates.

We present our age and distance estimates for NGC 6362 and NGC 6723 in Table 7. Their random uncertainties are calculated as standard deviations from 11 and 10 optical CMDs for NGC 6362 and NGC 6723, respectively. The right column presents the mean value and standard deviation of one measurement for the combined results of the two models. The standard deviations for the models and for the mean values are consistent, whereas the distributions of the combined results are Gaussian. This indicates good agreement

Table 7. Our NGC 6362 and NGC 6723 age (Gyr) and distance (kpc) estimates from optical CMDs. All the uncertainties are standard deviations of one measurement.

	DSED	BaSTI	Mean value
		NGC 6362	
Mean distance	7.76 ± 0.09	7.74 ± 0.16	7.75 ± 0.13
Mean age	12.00 ± 0.50	12.00 ± 0.50	12.00 ± 0.49
		NGC 6723	
Mean distance	8.14 ± 0.23	8.15 ± 0.18	8.15 ± 0.20
Mean age	12.35 ± 0.34	12.50 ± 0.33	12.43 ± 0.34

between the models in their distances and ages. Therefore, our final, most probable estimates for NGC 6362 and NGC 6723, respectively, are as follows:

(i) age is $12.00 \pm 0.10 \pm 0.8$ and $12.43 \pm 0.08 \pm 0.8$ Gyr (statistic and systematic uncertainties),

(ii) distance is $7.75 \pm 0.03 \pm 0.15$ and $8.15 \pm 0.04 \pm 0.15$ kpc,

(iii) distance modulus $(m - M)_0$ is $14.45 \pm 0.01 \pm 0.04$ and $14.56 \pm 0.01 \pm 0.04$ mag,

(iv) apparent V-band distance modulus $(m - M)_V$ is $14.64 \pm 0.03 \pm 0.06$ and $14.80 \pm 0.03 \pm 0.06$ mag.

Here, the random uncertainties equal the standard deviations of the combined samples divided by the square root of the number of the CMDs and models used (11 CMDs by 2 models and 10 CMDs by 2 models for NGC 6362 and NGC 6723, respectively).

Note that, in contrast to this study, DSED and BaSTI provided inconsistent age estimates in our previous papers. The reason is that the BaSTI isochrones were affected by a computational issue related to input physics and atomic diffusion treatment, which was solved a few months later (Cassisi, private communication). Hence, the BaSTI age estimates from our previous papers should be revisited.

Such a good agreement of the DSED and BaSTI estimates for both age and distance inspires our discussion of their systematic errors (see Section 3.1), which can be similar in both the models and, hence, should be considered separately. Systematic uncertainties of ± 0.15 kpc and 0.8 Gyr are assigned to our distance and age estimates, respectively. As noted in Section 3.1, since we adopt these systematic uncertainties from our study-to-study comparison, *a posteriori* comparison of our results with those from the studies has little sense. Therefore, the following comparison pays less attention to the literature estimates from isochrone-to-CMD studies, while more to other methods.

Our distance estimates agree with those from the recent compilation of all distance determinations by Baumgardt & Vasiliev (2021),[19] presented in Table 1, within 1.1σ and 0.8σ of their stated statistical uncertainties for NGC 6362 and NGC 6723, respectively, and even better – for the systematic uncertainties.

Note that both our and Baumgardt & Vasiliev (2021)'s estimates for NGC 6723 differ significantly from that of Harris (1996) (see Table 1). An impact of the Corona Australis cloud complex can be the reason for this difference in the distance estimates. Indeed, the distance estimate of Harris (1996) may be derived from the apparent magnitudes with underestimated extinction/reddening due to ignoring of the complex. In this case, the difference between our distance estimates and that of Harris (1996), i.e. $8700 - 8150 = 550$ pc, can be explained by the difference between the corresponding

distance moduli $14.70 - 14.56 = 0.14$ mag and, in turn, by the underestimation of extinction by $\Delta A_V = 0.14$ mag or reddening by $\Delta E(B - V) \approx 0.045$ mag. Such an underestimation can be easily explained by ignoring the differential reddening up to $\Delta E(B - V) \approx 0.13$ mag in the NGC 6723 field (see Section 4.4).

Our distance estimates can be converted into parallaxes for their comparison with other parallax estimates in Table 8 (the systematic uncertainty ± 0.15 kpc is assigned to our distances). An agreement within the stated uncertainties is seen. Anyway, the cluster distances from the *Gaia* parallaxes are still less accurate than those obtained from such an isochrone fitting.

Our age estimates are within a wide variety of age estimates for these GCs from the literature. Some differences in these estimates may be due to different approaches. For example, Oliveira et al. (2020) fit the same *HST* ACS data with DSED and BaSTI to obtain age estimates of 13.6 ± 0.5 and 12.6 ± 0.6 Gyr for NGC 6362 and NGC 6723, respectively. The former agrees with our estimate much worse than the latter. The reason may be that, in contrast to our study, they fit only the SGB and bright MS. Hence, in fact, they estimate age using only the length of the SGB. Such an estimate may be biased by large systematics.

5.5 Reddening and extinction

Reddenings, derived from CMD isochrone fitting, depend on adopted [Fe/H]. For example, Kerber et al. (2018) show that a change of the adopted [Fe/H] from -1.15 to -1.08 for NGC 6362 is followed by a change of the resulting $E(B - V)$ from 0.066 to 0.053 mag. [Fe/H] uncertainty is one of the largest contributors of total systematic uncertainty of derived reddening and extinction. Its importance has been underestimated in the balance of reddening uncertainties in our previous papers. Now, we estimate the total systematic uncertainty of our reddening and extinction estimates at the level of $\sigma E(B - V) = 0.02$ and $\sigma A_V = 0.06$ mag. Consequently, for such GCs with rather low reddening and extinction, R_V or any other characteristic of empirical extinction law must be very uncertain, being a ratio of these uncertain quantities. In addition, we take into account that both the data and models are less accurate in the UV and IR than in the optical range. Therefore, we change our approach in deriving reddening and extinction w.r.t. our previous papers.

Specifically, we derive our reddening and extinction estimates for each pair of a data set and a model from their most informative and precise CMDs, i.e. those presenting the longest optical wavelength range for each data set. For both the clusters, these are the CMDs with the following colours: $F606W$–$F814W$ for *HST* ACS; $F439W$–$F555W$ for *HST* WFPC2; $G_{BP} - G_{RP}$ for *Gaia* EDR3; $B - I$ for SPZ19; and $g_{SMSS} - z_{SMSS}$ for SMSS. In addition, for NGC 6362, we use $B - V$ from ZKR12 and NKP17, whereas for NGC 6723, we use $V - J_{2MASS}$ from HSV12, and $b - y$ from Lee (2019). Thus, we use seven data sets for each cluster. In order to combine these reddening estimates into our final estimates, we use the CCM89 extinction law with $R_V = 3.1$.

Similar to our previous papers, we verify the usage of this law by combining all the derived reddening estimates into empirical extinction laws. Briefly, we cross-identify the data sets with the VISTA and unWISE data sets[20] and use their IR extinctions to calculate extinctions in all filters from the derived reddenings. For

---

[19]This compilation is so comprehensive that our distance estimates do not need a comparison with individual estimates from the literature.

[20]Except the data sets of Piotto et al. (2002) and HSV12. The latter uses 2MASS instead of VISTA or un*WISE*.

Table 8. Various parallax estimates (mas) for NGC 6362 and NGC 6723.

Parallax	NGC 6362	NGC 6723
Shao & Li (2019), *Gaia* DR2 astrometry	0.123 ± 0.025	0.119 ± 0.025
VB21, *Gaia* EDR3 astrometry	0.132 ± 0.011	0.129 ± 0.011
This study, *Gaia* EDR3 astrometry	0.123 ± 0.011	0.123 ± 0.011
This study, isochrone fitting	0.129 ± 0.002	0.123 ± 0.002

Table 9. The estimates of $E(B - V)$ by use of the various models. The model estimates are mean values for seven data sets with the standard deviations of the mean values. The final values are the averages of the models with their uncertainties as half the differences between the model estimates.

	NGC 6362	NGC 6723
BaSTI	0.047 ± 0.004	0.059 ± 0.004
DSED	0.066 ± 0.005	0.077 ± 0.006
Final value	0.056 ± 0.011	0.068 ± 0.009

Table 10. The relative estimates of the derived [Fe/H] (dex), distance (kpc), age (Gyr), and $E(B - V)$ (mag) in the sense 'NGC 6723 minus NGC 6362'. The mean values are shown with their uncertainties.

	DSED	BaSTI	Mean value
[Fe/H]	-0.039	-0.067	-0.053 ± 0.014
Distance	0.41	0.48	0.44 ± 0.04
Age	0.39	0.61	0.50 ± 0.11
$E(B - V)$	0.0070	0.0078	0.0074 ± 0.0016

example,

$$A_{\rm V} = (A_{\rm V} - A_{\rm W1}) + A_{\rm W1} = E(V - W1) + A_{\rm W1} \qquad (2)$$

which is derived from reddening $E(V - W1)$ and a reasonable estimate of very low extinction $A_{\rm W1}$.

Figs 14 and 15 show that the obtained empirical extinction laws agree with the CCM89 extinction law when $R_{\rm V} = 3.1$. Also, Figs 14 and 15 act as crucial verifiers of the systematic agreement of different data sets within few hundredths of a magnitude. Indeed, the data sets show a low scatter around the extinction law curve. The only issue is a slight inconsistency between the *HST* ACS and WFC3 filters, providing a fracture in the *HST* empirical extinction law between the *F*438*W* and *F*606*W* filters (see Section 5.1). As noted earlier, this forces us to exclude the WFC3 filters from any final estimate.

The final reddening estimates are presented in Table 9. It is seen that the DSED estimates are systematically higher than their BaSTI equivalents by about 0.02 mag. This is due to systematically lower [Fe/H] of the DSED best-fitting isochrones (see Section 5.3).

A systematic uncertainty of ± 0.02 mag is assigned to our final $E(B - V)$ estimates (see Section 3.1). This is about twice as large as half the differences between the model estimates in Table 9. Accordingly, the systematic uncertainty of ± 0.06 mag is assigned to our final extinction estimates $A_{\rm V} = 0.19$ and 0.24 mag for NGC 6362 and NGC 6723, respectively. Here, we use the ratio $A_{\rm V} = 3.48E(B - V)$, taking into account intrinsic spectral energy distribution of rather cool and metal-poor stars of GCs (see Casagrande & VandenBerg 2014). It is worth noting that for NGC 6723, these are the reddening and extinction estimates at the centre of its field. Its differential reddening (see Section 4.4) should be taken into account for a proper estimate for a star or a part of the field. Note that a similar level of the reddening precision in Table 9 for NGC 6362 and NGC 6723 confirms our account of differential reddening.

Our $A_{\rm V}$ estimates are lower than those from Wagner-Kaiser et al. (2017), who use a Bayesian single-population analysis for the *HST* ACS data and obtain $A_{\rm V} = 0.248^{+0.001}_{-0.002}$ and $0.286^{+0.002}_{-0.002}$ for NGC 6362 and NGC 6723, respectively. However, our $A_{\rm V}$ estimates are higher than those from Valcin et al. (2020), who use isochrone fitting of the *HST* ACS data by DSED and obtain $A_{\rm V} = 0.16 \pm 0.02$ and 0.20 ± 0.03 for NGC 6362 and NGC 6723, respectively. The estimates of these studies are inconsistent each other. Yet, our large systematic uncertainty allows our estimates to be consistent with both of them.

Our $E(B - V)$ estimates agree with those from the isochrone fitting of the same or similar *HST* data with DSED by Dotter et al. (2010): $E(B - V) = 0.070$ for NGC 6362 and 0.073 for NGC 6723; with DSED and BaSTI, but only using the SGB and MS, by Oliveira et al. (2020): $E(B - V) = 0.04 \pm 0.01$ for NGC 6362 and 0.06 ± 0.01 for NGC 6723; with DSED and BaSTI by Kerber et al. (2018): $E(B - V) = 0.07 \pm 0.01$ for NGC 6362; and with a different model by VandenBerg et al. (2013): $E(B - V) = 0.076$ for NGC 6362 and 0.070 for NGC 6723.

As noted in Section 5.3, our reddening estimates agree with those obtained for cluster RR Lyrae stars by Arellano Ferro et al. (2018) ($E(B - V) = 0.063 \pm 0.024$ for NGC 6362) and Lee et al. (2014) ($E(B - V) = 0.061 \pm 0.014$ for NGC 6723).

We compare our $E(B - V)$ estimates with those in Table 1. For NGC 6362, our estimate is near the lowest estimate of Schlafly & Finkbeiner (2011), albeit comparable with that of SFD98. The reason for the deviation of our estimate from those of Harris (1996) and Meisner & Finkbeiner (2015) is not known. However, the inconsistency of the estimates of SFD98 and Meisner & Finkbeiner (2015), both calibrated from dust emission, may suggest a gradient of dust temperature or other inhomogeneity of the dust medium in the NGC 6362 field. For NGC 6723, our estimate agrees with only that of Harris (1996), which is apparently related to a majority of the cluster members and, hence, to the centre of the cluster. Naturally, our estimate is much lower than those from Schlafly & Finkbeiner (2011), SFD98, and Meisner & Finkbeiner (2015), which represent the whole cluster field with the reddening rise to its southern periphery.

5.6 Relative estimates and second parameter

As noted earlier, NGC 6362 and NGC 6723 are rich in precise photometry presented in the twin data sets. We use nine independent optical CMDs to derive relative (in the sense 'NGC 6723 minus NGC 6362') estimates of [Fe/H], distance, age, and $A_{\rm V}$ from isochrone fitting to each data set separately for each model. Other CMDs are eliminated from this procedure, since they engage the UV or IR filters. The only eliminated independent optical CMD, with the *F*438*W*–*F*606*W* colour, has the issue discussed in Section 5.1. The models are consistent in their relative estimates, which are presented in Table 10.

For each parameter, we calculate two kinds of uncertainty: half the difference between the BaSTI and DSED estimates and standard deviation of the mean value calculated as standard deviation of the

combined sample (both BaSTI and DSED estimates) divided by the square root of the estimates. The latter makes sense, since the distribution of such a combined sample by each parameter is nearly Gaussian. The largest among two uncertainties is adopted as the final uncertainty of each parameter in Table 10. As expected, the relative estimates are close to the differences between the absolute estimates, but they are much more precise, as seen from Table 10: NGC 6723 is 0.44 ± 0.04 kpc further, 0.5 ± 0.1 Gyr older, $\Delta E(B - V) = 0.007 \pm 0.002$ more reddened, and with 0.05 ± 0.01 dex lower [Fe/H] than NGC 6362. These uncertainties emphasize very high sensitivity of our approach.

The lower metallicity of NGC 6723 w.r.t. NGC 6362 is manifested in their different RGB slopes (see e.g. Fig. 13). The higher age of NGC 6723 w.r.t. NGC 6362 is manifested in their different SGB lengths and HB–SGB magnitude differences (see e.g. Figs 10). Such a combination of age and metallicity explains the difference in the HB morphology of these clusters mentioned in Section 2: NGC 6362 and NGC 6723 are richer in red and blue HB stars, respectively, and NGC 6723 has a longer blue hook of very hot HB stars, as seen in CMDs. This HB morphology difference can be expressed as the HB types[21] of these clusters (-0.08 for NGC 6362 and -0.58 for NGC 6723 from Mackey & van den Bergn 2005), or as their median colour difference between the HB and RGB ($\Delta(V - I) = 0.247 \pm 0.012$ for NGC 6362 and 0.371 ± 0.039 for NGC 6723 from Dotter et al. 2010). Both these characteristics represent a bluer HB of NGC 6723.

Both lower metallicity and higher age amplify the HB morphology difference, making the NGC 6723's HB bluer. Thus, all known parameters of these clusters, including our relative age and metallicity estimates, suggest that age is the second parameter for these clusters.

6 CONCLUSIONS

This study generally follows Paper I, Paper II, and Paper III in their approach to estimate some key parameters of Galactic globular clusters by fitting model isochrones to multiband photometry. To verify the sensitivity of our approach, we have considered the pair NGC 6362 and NGC 6723 with similar metallicity, distance, age, and extinction. In addition to distance, age, and extinction in various bands as the parameters in our previous studies, we also derived [Fe/H] of the clusters through isochrone fitting of the slope of the RGB in some CMDs. The obtained metallicities, [Fe/H] $= -1.04 \pm 0.07$ and -1.09 ± 0.06 for NGC 6362 and NGC 6723, respectively, agree with the spectroscopic estimates from the literature.

We used the photometry in 22 and 26 filters for NGC 6362 and NGC 6723, respectively, from the *HST*, *Gaia* EDR3, SMSS DR3, VISTA VHS DR5, unWISE, and other data sets. These filters span a wavelength range from about 230 to 4060 nm, i.e. from the UV to mid-IR. As in our previous studies, some data sets were cross-identified with each other. This allowed us to (i) estimate systematic differences of the data sets and (ii) use the VISTA and unWISE photometry with nearly zero extinction for determination of extinction in all other filters and verification of agreement of the empirical extinction laws with the CCM89 law when $R_V = 3.1$.

As in Paper III, to fit the data, we used the DSED and BaSTI theoretical models of stellar evolution for α-enriched populations with primordial and enhanced helium abundance. The models differ in their physics and predictions for [Fe/H] and reddening, but those for age and distance are consistent. DSED provides [Fe/H] that is about 0.12 dex systematically lower than BaSTI and $\Delta E(B - V) \approx 0.02$ mag systematically higher than BaSTI.

For NGC 6362 and NGC 6723, we derived the distances $7.75 \pm 0.03 \pm 0.15$ and $8.15 \pm 0.04 \pm 0.15$ kpc (statistic and systematic uncertainties), distance moduli $14.45 \pm 0.01 \pm 0.04$ and $14.56 \pm 0.01 \pm 0.04$ mag, apparent *V*-band distance moduli $14.64 \pm 0.03 \pm 0.06$ and $14.80 \pm 0.03 \pm 0.06$ mag, ages $12.00 \pm 0.10 \pm 0.80$ and $12.43 \pm 0.08 \pm 0.80$ Gyr, extinctions $A_V = 0.19 \pm 0.04 \pm 0.06$ and $0.24 \pm 0.03 \pm 0.06$ mag, and reddenings $E(B - V) = 0.056 \pm 0.01 \pm 0.02$ and $0.068 \pm 0.01 \pm 0.02$ mag, respectively.

The use of the twin data sets from *Gaia* EDR3, SMSS, SPZ19, Nardiello et al. (2018), and Piotto et al. (2002), for both the clusters allowed us to obtain very precise relative estimates of the parameters. We found that NGC 6723 is 0.44 ± 0.04 kpc further, 0.5 ± 0.1 Gyr older, $\Delta E(B - V) = 0.007 \pm 0.002$ more reddened, and with 0.05 ± 0.01 dex lower [Fe/H] than NGC 6362. These uncertainties show a high sensitivity of our approach. These differences in age and metallicity explain the difference of the HB morphology between these clusters. This suggests age as the second parameter for NGC 6362 and NGC 6723.

We found a strong differential reddening of about $\Delta E(B - V) \approx 0.14$ mag across 17 arcmin of the field of NGC 6723 due to its proximity to the Corona Australis cloud complex. This differential reddening may explain a large diversity of the reddening/extinction estimates for NGC 6723 from the literature. Moreover, the influence of the complex can explain the apparently wrong estimate of the NGC 6723 distance in the data base of Harris (1996).

Using the *Gaia* EDR3 data, we provided the lists of reliable members of the clusters and systemic PMs with their total (systematic plus random) uncertainties in mas yr^{-1}:

$$\mu_\alpha \cos(\delta) = -5.512 \pm 0.024, \ \mu_\delta = -4.780 \pm 0.024$$
$$\mu_\alpha \cos(\delta) = 1.021 \pm 0.026, \ \mu_\delta = -2.427 \pm 0.026$$

for NGC 6362 and NGC 6723, respectively.

---

[21]The HB type is defined as $(N_B - N_R)/(N_B + N_V + N_R)$, where N_B, N_V, and N_R are the number of stars that lie blueward of the instability strip, the number of RR Lyrae variables, and the number of stars that lie redward of the instability strip, respectively (Lee, Demarque & Zinn 1994).

This study make use of data from the Cerro Tololo Inter-American Observatory 1 m telescope, which is operated by the SMARTS consortium. This research makes use of Filtergraph (Burger et al. 2013), an online data visualization tool developed at Vanderbilt University through the Vanderbilt Initiative in Data-intensive Astrophysics (VIDA) and the Frist Center for Autism and Innovation (FCAI, https://filtergraph.com). The resources of the Centre de Données astronomiques de Strasbourg, Strasbourg, France (http://cds.u-strasbg.fr), including the SIMBAD database, the VizieR catalogue access tool and the X-Match service, were widely used in this study. This work has made use of BaSTI and DSED web tools. This work makes use of data from the European Space Agency (ESA) mission *Gaia* (https://www.cosmos.esa.int/gaia), processed by the *Gaia* Data Processing and Analysis Consortium (DPAC, https://www.cosmos.esa.int/web/gaia/dpac/consortium). The Gaia archive website is https://archives.esac.esa.int/gaia. This study is based on observations made with the NASA/ESA *Hubble Space Telescope*. This publication makes use of data products from the *Wide-field Infrared Survey Explorer*, which is a joint project of the University of California, Los Angeles, and the Jet Propulsion Laboratory/California Institute of Technology. This publication makes use of data products from the Pan-STARRS Surveys (PS1). This study makes use of data products from the SkyMapper Southern Sky Survey. SkyMapper is owned and operated by The Australian National University's Research School of Astronomy and Astrophysics. The SkyMapper survey data were processed and provided by the SkyMapper Team at ANU. The SkyMapper node of the All-Sky Virtual Observatory (ASVO) is hosted at the National Computational Infrastructure (NCI).

DATA AVAILABILITY

The data underlying this article will be shared on reasonable request to the corresponding author.

REFERENCES

Alcaino G., Liller W., Alvarado F., Mironov A., Ipatov A., Piskunov A., Samus N., Smirnov O., 1999, A&AS, 136, 461 (ALA99)

Anderson J. et al., 2008, AJ, 135, 2055

Arellano Ferro A., Ahumada J. A., Bustos Fierro I. H., Calderón J. H., Morrell N. I., 2018, Astron. Nachr., 339, 183

Baumgardt H., Vasiliev E., 2021, MNRAS, 505, 5957

Bica E., Pavani D. B., Bonatto C. J., Lima E. F., 2019, AJ, 157, 12

Bonatto C., Campos F., Kepler S. O., 2013, MNRAS, 435, 263 (BCK13)

Brocato E., Castellani V., Raimondo G., Walker A. R., 1999, ApJ, 527, 230

Burger D., Stassun K. G., Pepper J., Siverd R. J., Paegert M., De Lee N. M., Robinson W. H., 2013, Astron. Comput., 2, 40

Cardelli J. A., Clayton G. C., Mathis J. S., 1989, ApJ, 345, 245 (CCM89)

Carretta E., Bragaglia A., Gratton R., D'Orazi V., Lucatello S., 2009, A&A, 508, 695

Casagrande L., VandenBerg Don A., 2014, MNRAS, 444, 392

Casagrande L., VandenBerg Don A., 2018a, MNRAS, 475, 5023

Casagrande L., VandenBerg Don A., 2018b, MNRAS, 479, L102

Crestani J., Alves-Brito A., Bono G., Puls A. A., Alonso-Garcia J., 2019, MNRAS, 487, 5463

Dalessandro E. et al., 2014, ApJ, 791, L4

Dotter A., Chaboyer B., Jevremović D., Baron E., Ferguson J. W., Sarajedini A., Anderson J., 2007, AJ, 134, 376

Dotter A., Chaboyer B., Jevremović D., Kostov V., Baron E., Ferguson J. W., 2008, ApJS, 178, 89

Dotter A. et al., 2010, ApJ, 708, 698

Evans D. W. et al., 2018, A&A, 616, A4

Goldsbury R., Richer H. B., Anderson J., Dotter A., Sarajedini A., Woodley K., 2010, AJ, 140, 1830

Gontcharov G. A., Mosenkov A. V., Khovritchev M. Yu., 2019, MNRAS, 483, 4949 (Paper I)

Gontcharov G. A., Mosenkov A. V., Khovritchev M. Yu., 2020, MNRAS, 497, 3674 (Paper II)

Gontcharov G. A. et al., 2021, MNRAS, 508, 2688 (Paper III)

Gratton R. G. et al., 2015, A&A, 573, A92

Harris W. E., 1996, AJ, 112, 1487

Heber U., 2016, PASP, 128, 082001

Hendricks B., Stetson P. B., VandenBerg D. A., Dall'Ora M., 2012, AJ, 144, 25 (HSV12)

Hewett P. C., Warren S. J., Leggett S. K., Hodgkin S. T., 2006, MNRAS, 367, 454

Hidalgo S. L. et al., 2018, ApJ, 856, 125

Kaluzny J., Thompson I. B., Dotter A., Rozyczka M., Schwarzenberg-Czerny A., Burley G. S., Mazur B., Rucinski S. M., 2015, AJ, 150, 155

Kerber L. O., Nardiello D., Ortolani S., Barbuy B., Bica E., Cassisi S., Libralato M., Vieira R. G., 2018, ApJ, 853, 15

Lagioia E. P. et al., 2018, MNRAS, 475, 4088

Lee J. W., López-Morales M., Hong K., Kang Y.-W., Pohl B. L., Walker A., 2014, ApJS, 210, 6

Lee J.-W., 2019, ApJ, 883, 166

Lee Y.-W., Demarque P., Zinn R., 1994, ApJ, 423, 248

Lindegren L. et al., 2021a, A&A, 649, A2

Lindegren L. et al., 2021b, A&A, 649, A4

Mackey A. D., van den Bergh S., 2005, MNRAS, 360, 631

Massari D. et al., 2017, MNRAS, 468, 1249

McMahon R. G., Banerji M., Gonzalez E., Koposov S. E., Bejar V. J., Lodieu N., Rebolo R., VHS Collab., 2013, The Messenger, 154, 35

Meisner A. M., Finkbeiner D. P., 2015, ApJ, 798, 88

Milone A. P. et al., 2017, MNRAS, 464, 3636

Milone A. P. et al., 2018, MNRAS, 481, 5098

Monelli M. et al., 2013, MNRAS, 431, 2126

Mucciarelli A. et al., 2016, ApJ, 824, 73

Nardiello D. et al., 2018, MNRAS, 481, 3382

Narloch W., Kaluzny J., Poleski R., Rozyczka M., Pych W., Thompson I. B., 2017, MNRAS, 471, 1446 (NKP17)

O'Malley E. M., Gilligan C., Chaboyer B., 2017, ApJ, 838, 162

Ochsenbein F., Bauer P., Marcout J., 2000, A&AS, 143, 221

Oliveira R. A. P. et al., 2020, ApJ, 891, 37

Onken C. A. et al., 2019, PASA, 36, 33

Paust N. E. Q. et al., 2010, AJ, 139, 476

Pietrinferni A. et al., 2021, ApJ, 908, 102

Piotto G. et al., 1999, AJ, 117, 264

Piotto G. et al., 2002, A&A, 391, 945

Piotto G. et al., 2015, AJ, 149, 91

Reimers D., 1975, Mem. Soc. R. Sci. Liege, 8, 369

Riello M. et al., 2021, A&A, 649, A3

Rojas-Arriagada A., Zoccali M., Vasquez S., Ripepi V., Musella I., Marconi M., Grado A., Limatola L., 2016, A&A, 587, A95

Savino A., Massari D., Bragaglia A., Dalessandro E., Tolstoy E., 2018, MNRAS, 474, 4438

Schlafly E. F., Finkbeiner D. P., 2011, ApJ, 737, 103

Schlafly E. F., Meisner A. M., Green G. M., 2019, ApJS, 240, 30

Schlegel D. J., Finkbeiner D. P., Davis M., 1998, ApJ, 500, 525(SFD98)

Shao Z., Li L., 2019, MNRAS, 489, 3093

Simioni M. et al., 2018, MNRAS, 476, 271

Skrutskie M. F. et al., 2006, AJ, 131, 1163

Stetson P. B., Pancino E., Zocchi A., Sanna N., Monelli M., 2019, MNRAS, 485, 3042 (SPZ19)

Tailo M. et al., 2020, MNRAS, 498, 5745

Valcin D., Bernal J. L., Jimenez R., Verde L., Wandelt B. D., 2020, J. Cosmol. Astropart. Phys., 12, 2

VandenBerg Don A., Denissenkov P. A., 2018, ApJ, 862, 72

VandenBerg Don A., Brogaard K., Leaman R., Casagrande L., 2013, ApJ, 775, 134

VandenBerg Don A., Casagrande L., Edvardsson B., 2022, MNRAS, 509, 4208

Vasiliev E., Baumgardt H., 2021, MNRAS, 505, 5978 (VB21)

Vitral E., 2021, MNRAS, 504, 1355

Wagner-Kaiser R. et al., 2016, MNRAS, 463, 3768

Wagner-Kaiser R. et al., 2017, MNRAS, 468, 1038

Wright E. L. et al., 2010, AJ, 140, 1868

Zloczewski K., Kaluzny J., Rozyczka M., Krzeminski W., Mazur B., 2012, Acta Astron., 62, 357 (ZKR12)

SUPPORTING INFORMATION

Supplementary data are available at *MNRAS* online.

gontcharov_tables_new.zip

suppl_data

Please note: Oxford University Press is not responsible for the content or functionality of any supporting materials supplied by the authors. Any queries (other than missing material) should be directed to the corresponding author for the article.
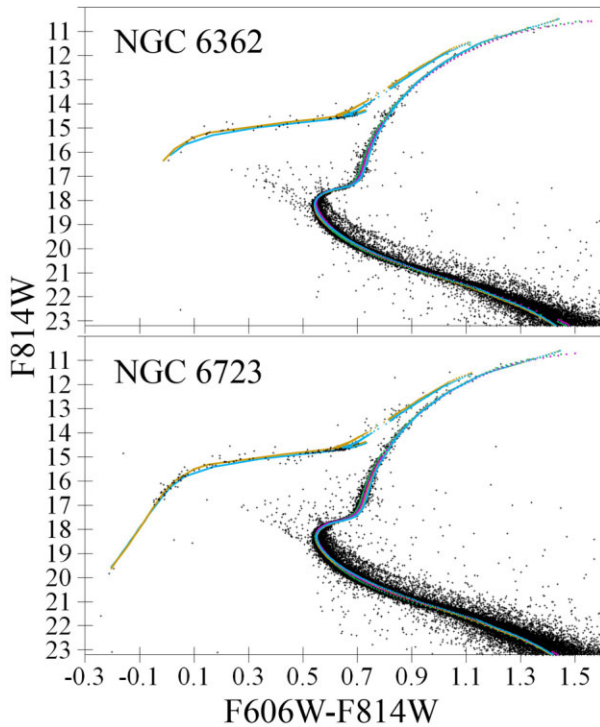
APPENDIX A: SOME CMDS OF NGC 6362 AND NGC 6723

Figure A1. The CMDs for NGC 6362 and NGC 6723 with the *HST* ACS *F*606*W–F*814*W* colour. The isochrones from BaSTI for $Y \approx 0.25$ (blue) and 0.275 (brown) and from DSED for $Y \approx 0.25$ (purple) and 0.275 (green) are calculated with the best-fitting parameters from Table 6. The HB of NGC 6723 is extended in the blue direction to show that two very hot stars may be HB members of the cluster.
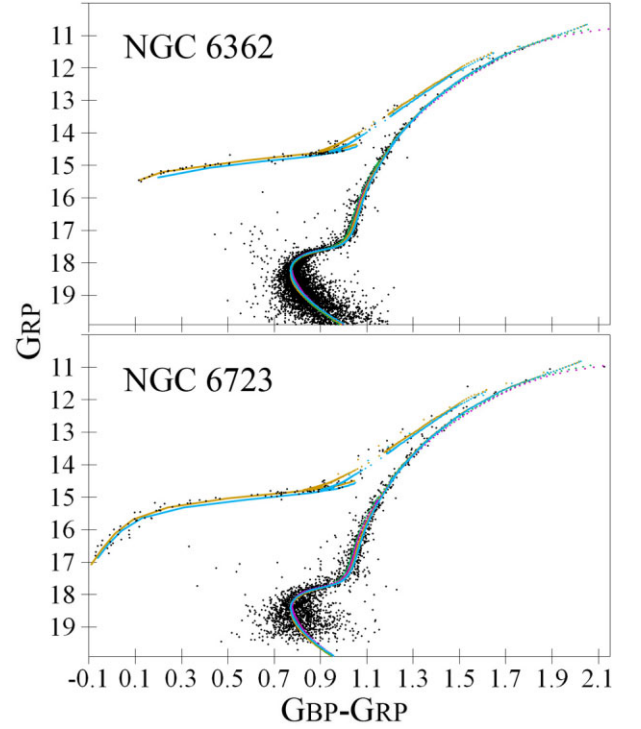

Figure A2. The same as Fig. A1 but for the *Gaia* EDR3 $G_{BP}-G_{RP}$ colour.
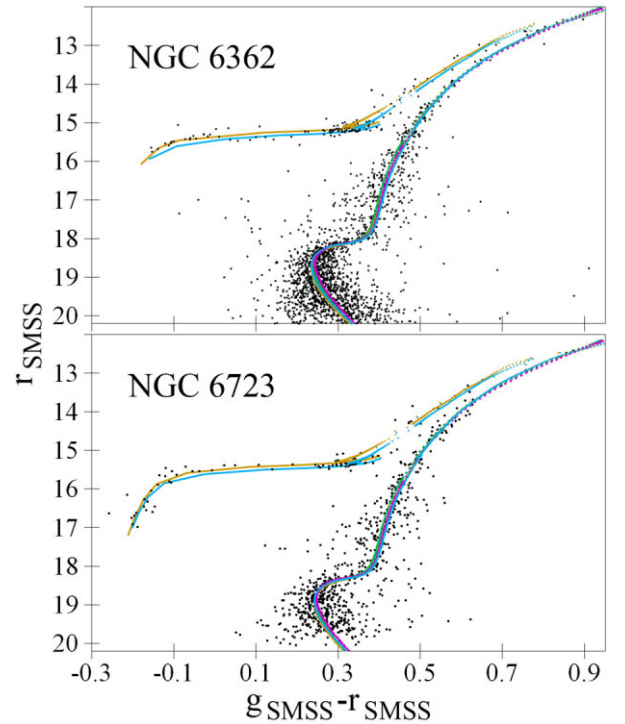

Figure A3. The same as Fig. A1 but for the SMSS $g_{SMSS}-r_{SMSS}$ colour.

This paper has been typeset from a TeX/LaTeX file prepared by the author.

List of astronomical key words (Updated on 2020 January)

This list is common to *Monthly Notices of the Royal Astronomical Society, Astronomy and Astrophysics*, and *The Astrophysical Journal*. In order to ease the search, the key words are subdivided into broad categories. No more than *six* subcategories altogether should be listed for a paper.

 The subcategories in boldface containing the word 'individual' are intended for use with specific astronomical objects; these should never be used alone, but always in combination with the most common names for the astronomical objects in question. Note that each object counts as one subcategory within the allowed limit of six.

 The parts of the key words in italics are for reference only and should be omitted when the keywords are entered on the manuscript.

General
editorials, notices
errata, addenda
extraterrestrial intelligence
history and philosophy of astronomy
miscellaneous
obituaries, biographies
publications, bibliography
sociology of astronomy
standards

Physical data and processes
acceleration of particles
accretion, accretion discs
asteroseismology
astrobiology
astrochemistry
astroparticle physics
atomic data
atomic processes
black hole physics
chaos
conduction
convection
dense matter
diffusion
dynamo
elementary particles
equation of state
gravitation
gravitational lensing: micro
gravitational lensing: strong
gravitational lensing: weak
gravitational waves
hydrodynamics
instabilities
line: formation
line: identification
line: profiles
magnetic fields
magnetic reconnection
(magnetohydrodynamics) MHD
masers
molecular data
molecular processes
neutrinos
nuclear reactions, nucleosynthesis, abundances
opacity
plasmas
polarization

radiation: dynamics
radiation mechanisms:general
radiation mechanisms: non-thermal
radiation mechanisms: thermal
radiative transfer
relativistic processes
scattering
shock waves
solid state: refractory
solid state: volatile
turbulence
waves

Astronomical instrumentation, methods and techniques
atmospheric effects
balloons
instrumentation: adaptive optics
instrumentation: detectors
instrumentation: high angular resolution
instrumentation: interferometers
instrumentation: miscellaneous
instrumentation: photometers
instrumentation: polarimeters
instrumentation: spectrographs
light pollution
methods: analytical
methods: data analysis
methods: laboratory: atomic
methods: laboratory: molecular
methods: laboratory: solid state
methods: miscellaneous
methods: numerical
methods: observational
methods: statistical
site testing
space vehicles
space vehicles: instruments
techniques: high angular resolution
techniques: image processing
techniques: imaging spectroscopy
techniques: interferometric
techniques: miscellaneous
techniques: photometric
techniques: polarimetric
techniques: radar astronomy
techniques: radial velocities
techniques: spectroscopic
telescopes

Astronomical data bases
astronomical data bases: miscellaneous
atlases
catalogues
surveys
virtual observatory tools

Software
software: data analysis
software: development
software: documentation
software: public release
software: simulations

Astrometry and celestial mechanics
astrometry
celestial mechanics
eclipses
ephemerides
occultations
parallaxes
proper motions
reference systems
time

The Sun
Sun: abundances
Sun: activity
Sun: atmosphere
Sun: chromosphere
Sun: corona
Sun: coronal mass ejections (CMEs)
Sun: evolution
Sun: faculae, plages
Sun: filaments, prominences
Sun: flares
Sun: fundamental parameters
Sun: general
Sun: granulation
Sun: helioseismology
Sun: heliosphere
Sun: infrared
Sun: interior
Sun: magnetic fields
Sun: oscillations
Sun: particle emission
Sun: photosphere
Sun: radio radiation
Sun: rotation
(Sun:) solar–terrestrial relations
(Sun:) solar wind
(Sun:) sunspots
Sun: transition region
Sun: UV radiation
Sun: X-rays, gamma-rays

Planetary systems
comets: general

comets: individual: . . .
Earth
interplanetary medium
Kuiper belt: general

Kuiper belt objects: individual: . . .
meteorites, meteors, meteoroids

minor planets, asteroids: general
minor planets, asteroids: individual: . . .
Moon
Oort Cloud
planets and satellites: atmospheres
planets and satellites: aurorae
planets and satellites: composition
planets and satellites: detection
planets and satellites: dynamical evolution and stability
planets and satellites: formation
planets and satellites: fundamental parameters
planets and satellites: gaseous planets
planets and satellites: general

planets and satellites: individual: . . .
planets and satellites: interiors
planets and satellites: magnetic fields
planets and satellites: oceans
planets and satellites: physical evolution
planets and satellites: rings
planets and satellites: surfaces
planets and satellites: tectonics
planets and satellites: terrestrial planets
planet–disc interactions
planet–star interactions
protoplanetary discs
zodiacal dust

Stars
stars: abundances
stars: activity
stars: AGB and post-AGB
stars: atmospheres
(stars:) binaries *(including multiple)*: close
(stars:) binaries: eclipsing
(stars:) binaries: general
(stars:) binaries: spectroscopic
(stars:) binaries: symbiotic
(stars:) binaries: visual
stars: black holes
(stars:) blue stragglers
(stars:) brown dwarfs
stars: carbon
stars: chemically peculiar
stars: chromospheres
(stars:) circumstellar matter
stars: coronae
stars: distances
stars: dwarf novae
stars: early-type
stars: emission-line, Be
stars: evolution
stars: flare
stars: formation
stars: fundamental parameters
(stars:) gamma-ray burst: general
(stars:) **gamma-ray burst: individual: . . .**
stars: general
(stars:) Hertzsprung–Russell and colour–magnitude diagrams
stars: horizontal branch
stars: imaging
stars: individual: . . .
stars: interiors

stars: jets
stars: kinematics and dynamics
stars: late-type
stars: low-mass
stars: luminosity function, mass function
stars: magnetars
stars: magnetic fields
stars: massive
stars: mass-loss
stars: neutron
(stars:) novae, cataclysmic variables
stars: oscillations *(including pulsations)*
stars: peculiar *(except chemically peculiar)*
(stars:) planetary systems
stars: Population II
stars: Population III
stars: pre-main-sequence
stars: protostars
(stars:) pulsars: general
(stars:) **pulsars: individual: . . .**
stars: rotation
stars: solar-type
(stars:) starspots
stars: statistics
(stars:) subdwarfs
(stars:) supergiants
(stars:) supernovae: general
(stars:) **supernovae: individual: . . .**
stars: variables: Cepheids
stars: variables: Scuti
stars: variables: general
stars: variables: RR Lyrae
stars: variables: S Doradus
stars: variables: T Tauri, Herbig Ae/Be
(stars:) white dwarfs
stars: winds, outflows
stars: Wolf–Rayet

Interstellar medium (ISM), nebulae
ISM: abundances
ISM: atoms
ISM: bubbles
ISM: clouds
(ISM:) cosmic rays
(ISM:) dust, extinction
ISM: evolution
ISM: general
(ISM:) HII regions
(ISM:) Herbig–Haro objects

ISM: individual objects: . . .
(except planetary nebulae)
ISM: jets and outflows
ISM: kinematics and dynamics
ISM: lines and bands
ISM: magnetic fields
ISM: molecules
(ISM:) photodissociation region (PDR)
(ISM:) planetary nebulae: general
(ISM:) **planetary nebulae: individual: . . .**
ISM: structure
ISM: supernova remnants

The Galaxy
Galaxy: abundances
Galaxy: bulge
Galaxy: centre
Galaxy: disc
Galaxy: evolution
Galaxy: formation
Galaxy: fundamental parameters
Galaxy: general
(Galaxy:) globular clusters: general
(Galaxy:) **globular clusters: individual: . . .**
Galaxy: halo
Galaxy: kinematics and dynamics
(Galaxy:) local interstellar matter
Galaxy: nucleus
(Galaxy:) open clusters and associations: general
(Galaxy:) **open clusters and associations: individual: . . .**
(Galaxy:) solar neighbourhood
Galaxy: stellar content
Galaxy: structure

Galaxies
galaxies: abundances
galaxies: active
galaxies: bar
(galaxies:) BL Lacertae objects: general
(galaxies:) **BL Lacertae objects: individual: . . .**
galaxies: bulges
galaxies: clusters: general

galaxies: clusters: individual: . . .
galaxies: clusters: intracluster medium
galaxies: disc
galaxies: distances and redshifts
galaxies: dwarf
galaxies: elliptical and lenticular, cD
galaxies: evolution
galaxies: formation
galaxies: fundamental parameters
galaxies: general
galaxies: groups: general

galaxies: groups: individual: . . .
galaxies: haloes
galaxies: high-redshift

galaxies: individual: . . .
galaxies: interactions
(galaxies:) intergalactic medium
galaxies: irregular
galaxies: ISM
galaxies: jets
galaxies: kinematics and dynamics
(galaxies:) Local Group
galaxies: luminosity function, mass function
(galaxies:) Magellanic Clouds
galaxies: magnetic fields
galaxies: nuclei
galaxies: peculiar
galaxies: photometry
(galaxies:) quasars: absorption lines
(galaxies:) quasars: emission lines
(galaxies:) quasars: general

(galaxies:) **quasars: individual: . . .**
(galaxies:) quasars: supermassive black holes
galaxies: Seyfert
galaxies: spiral
galaxies: starburst
galaxies: star clusters: general

galaxies: star clusters: individual: . . .
galaxies: star formation
galaxies: statistics
galaxies: stellar content
galaxies: structure

Cosmology
(cosmology:) cosmic background radiation
(cosmology:) cosmological parameters
 (cosmology:) dark ages, reionization, first stars
(cosmology:) dark energy
(cosmology:) dark matter
(cosmology:) diffuse radiation
(cosmology:) distance scale
(cosmology:) early Universe
(cosmology:) inflation
(cosmology:) large-scale structure of Universe
cosmology: miscellaneous
cosmology: observations
(cosmology:) primordial nucleosynthesis
cosmology: theory

Resolved and unresolved sources as a function of wavelength
gamma-rays: diffuse background
gamma-rays: galaxies
gamma-rays: galaxies: clusters
gamma-rays: general
gamma-rays: ISM
gamma-rays: stars
infrared: diffuse background
infrared: galaxies
infrared: general
infrared: ISM
infrared: planetary systems
infrared: stars
radio continuum: galaxies
radio continuum: general
radio continuum: ISM
radio continuum: planetary systems
radio continuum: stars
radio continuum: transients
radio lines: galaxies
radio lines: general
radio lines: ISM
radio lines: planetary systems
radio lines: stars
submillimetre: diffuse background
submillimetre: galaxies
submillimetre: general
submillimetre: ISM
submillimetre: planetary systems
submillimetre: stars
ultraviolet: galaxies

ultraviolet: general
ultraviolet: ISM
ultraviolet: planetary systems
ultraviolet: stars
X-rays: binaries
X-rays: bursts
X-rays: diffuse background
X-rays: galaxies
X-rays: galaxies: clusters
X-rays: general
X-rays: individual: . . .
X-rays: ISM
X-rays: stars

Transients
(transients:) black hole mergers
(transients:) black hole - neutron star mergers
(transients:) fast radio bursts
(transients:) gamma-ray bursts
(transients:) neutron star mergers
transients: novae
transients: supernovae
transients: tidal disruption events